

Orbital Altermagnetism in Two Dimensions

Mingxiang Pan,¹ Feng Liu,^{2,*} and Huaqing Huang^{1,3,4,†}

¹*School of Physics, Peking University, Beijing 100871, China*

²*Department of Materials Science and Engineering,
University of Utah, Salt Lake City, Utah 84112, USA*

³*Collaborative Innovation Center of Quantum Matter, Beijing 100871, China*

⁴*Center for High Energy Physics, Peking University, Beijing 100871, China*

(Dated: March 11, 2026)

We introduce the concept of *orbital altermagnetism*, a symmetry-protected magnetic order of pure orbital degrees of freedom. It is characterized with ordered anti-parallel orbital magnetic moments in real space but momentum-dependent orbital band splittings, analogous to spin altermagnetism. Using a minimal tight-binding model with complex hoppings in a square-kagome lattice, we show that such order inherently arises from staggered loop currents, producing a *d*-wave-like orbital-momentum locking. First-principles calculations show that orbital altermagnetism emerges independent of spin ordering in in-plane ferromagnets of CuBr₂ and VS₂, so that it can be unambiguously identified experimentally. On the other hand, it may also coexist with spin altermagnetism, such as in monolayer MoO and CrO. The orbital altermagnetism offers an alternative platform for symmetry-driven magnetotransport and orbital-based spintronics, as exemplified by large nonlinear current-induced orbital magnetization.

Introduction.—Altermagnetism has recently emerged as a distinct class of magnetic order, fundamentally different from both conventional collinear ferromagnetism and antiferromagnetism [1–6]. Characterized by symmetry-protected, momentum-dependent alternating spin splitting in the band structure and collinear compensated magnetic moments in real space, altermagnets enable novel spin transport phenomena, such as giant and tunnelling magnetoresistance [7], nonrelativistic spin current generation [8–11], and nonlinear transports [12, 13]. These properties make them promising platforms for spintronics, offering high-speed and low-dissipation spin control without a net magnetization [14–24].

While magnetic order is usually pertained to spin degrees of freedom, orbital contributions to magnetism can be equally important. Ferromagnetic order formed by orbital magnetic moments has been reported in morié Chern insulators [25–31] and rhombohedral graphene superlattices [32–37]. Weak orbital ferromagnetism can even survive in spin antiferromagnets [38–41]. Another prominent example is the interaction-driven loop-current phase proposed in cuprates [42–50], where spontaneous circulating currents within a unit cell generate finite orbital moments. In a mean-field description, such states correspond to complex inter-orbital hopping amplitudes, breaking time-reversal symmetry and producing orbital antiferromagnetism independent of spin ordering. Also, interaction driven ordering has been proposed to interestingly promote spin altermagnetism [51]. These developments naturally raise a fundamental question: can local orbital magnetic moments *alone* form an altermagnetic state, in analogous to spin altermagnetism?

In this Letter, we introduce the concept of *orbital altermagnetism*—an altermagnetic order originating from staggered local orbital magnetic moments, namely, a

magnetic ordered phase of pure orbital degrees of freedom [52–54]. Using a minimal tight-binding model with spontaneously ordered loop currents, we demonstrate the emergence of a characteristic real-space pattern of anti-parallel orbital magnetic moments and a distinct feature of *d*-wave-like orbital-momentum locking in momentum space. Importantly, we show that orbital altermagnetism can exist independent of spin configurations in realistic materials. First-principles calculations reveal a definite manifestation of orbital altermagnetism in in-plane ferromagnets CuBr₂ and VS₂ with staggered out-of-plane orbital moments distinct from the uniform in-plane spin distributions. Furthermore, we find that conventional spin altermagnets can be accompanied with a hidden orbital altermagnetism, as exemplified by monolayer MoO and CrO, and we uncover a giant nonlinear current-induced orbital magnetization that far exceeds the spin contribution, which may serve as an experimental signature of the orbital altermagnetism.

Minimal model for 2D orbital altermagnetism.—We illustrate orbital altermagnetism using a minimal tight-binding model on a two-dimensional square-kagome lattice [55–57] with complex hoppings [Fig. 1(a)]. Each unit cell contains three nonequivalent sites, labeled A, B, and C. The A sites sit at edge centers, ($\frac{1}{2}, 0$) and ($0, \frac{1}{2}$), while B and C occupy positions of ($\frac{1}{2} \pm \tau, \frac{1}{2} \pm \tau$) and ($\frac{1}{2} \pm \tau, \frac{1}{2} \mp \tau$), respectively, with $\tau = 1/8$. The Hamiltonian reads

$$H = \sum_{\alpha,i} \epsilon_{\alpha} c_{\alpha i}^{\dagger} c_{\alpha i} + \sum_{\langle\langle i,j \rangle\rangle} t_1 (c_{A_i}^{\dagger} c_{B_j} + c_{A_i}^{\dagger} c_{C_j}) + \sum_{\langle i,j \rangle} t_2 e^{i\phi} c_{C_i}^{\dagger} c_{B_j} + \text{H.c.}, \quad (1)$$

where $c_{\alpha i}^{\dagger}$ ($c_{\alpha i}$) creates (annihilates) an electron on site i of type $\alpha = A, B, C$. The first term describes next-

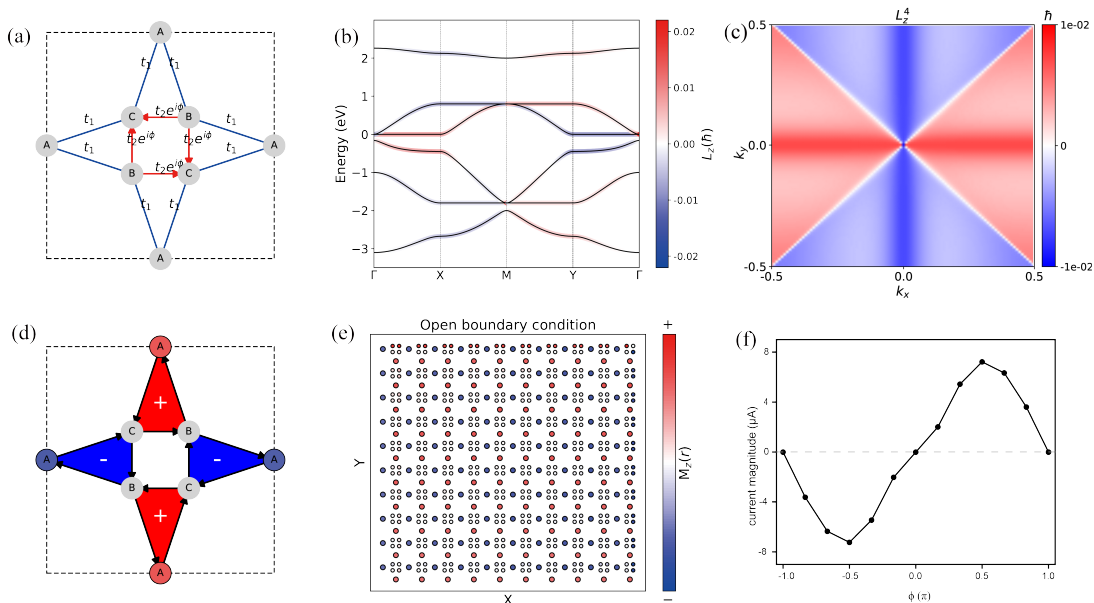


FIG. 1. (a) Unit cell (dashed box) of the tight-binding model described by Eq. (1) includes three types of sites labeled A, B, and C in a square-kagome lattice, respectively. The nearest-neighbor hopping $t_2 e^{i\phi}$ has a complex phase (red arrow), and next-nearest-neighbor hopping t_1 (blue) is real. Arrows indicate the direction of positive phase hopping. (b) Band structure of the model. (c) \mathbf{k} -space distribution of the orbital angular momentum L_z for the fourth band, with k_x and k_y in reduced coordinates. (d) Loop-current pattern in the model. Arrows indicate the calculated inter-site currents ($\sim 5.4 \mu\text{A}$), with red (+) and blue (-) regions denoting positive and negative z -components of the orbital magnetic moment M_z . (e) Real-space distribution of orbital magnetic moments in a 10×10 lattice under open boundary conditions at $\mu = 0$ eV. Red (blue) indicates a positive (negative) $M_z(\mathbf{r})$. (f) Inter-site current as a function of phase ϕ . Model parameters: $\epsilon_A = -1.0$, $\epsilon_{B/C} = 0$, $t_1 = -0.6$, $t_2 = -1.0$, and $\phi = \pi/3$.

nearest-neighbor hopping with amplitude t_1 , and the second term corresponds to nearest-neighbor hopping of amplitude t_2 with an orbital-dependent phase $e^{i\phi}$. The phase ϕ encodes the microscopic loop current pattern responsible for orbital altermagnetic order. The magnetic point group of this model, with the orbital moment acting like spins, is $4'/mm'm$, as verified from symmetry operations acting on the lattice with directed bonds.

We first compute the electronic structure and the orbital angular momentum L_z , which is directly proportional to the orbital magnetic moment $M_z = -\mu_B g_L L_z$ ($g_L = 1$) within the modern theory of orbital magnetization [58–64]. As shown in Fig. 1(b), the bands exhibit opposite L_z polarization along k_x and k_y . The momentum-space distribution of L_z [Fig. 1(c)] displays a characteristic L_z -momentum locking, analogous to the spin texture of d -wave spin altermagnets. The corresponding real-space orbital magnetization, computed from its Wannier-based expression [65–68], is shown in Fig. 1(e) for an open-boundary system. The real-space orbital moments, which are decomposed to lattice sites, are predominantly localized on A sites and opposite orientation in a Néel-antiferromagnetic-like pattern across the lattice, yielding a fully compensated configuration. Therefore, in analogy to spin altermagnetism, we refer to this state as *orbital altermagnetism*—characterized by a compensated real-

space arrangement and alternating momentum-space orbital splitting. The observed d -wave pattern is fully compatible with the magnetic space group, albeit with orbital-momentum locking in place of spin-momentum locking or spin-orbit coupling (SOC).

The underlying physics can be understood in terms of local loop currents. Figure 1(d) shows the bond-resolved current distribution, where black arrows indicate current flow. On each ABC triangle, a current of magnitude $\sim 5.4 \mu\text{A}$ circulates in the A-C-B direction, generating an out-of-plane orbital magnetic moment at the center of triangle. Neighboring triangles host counter-circulating loops, and hence antiparallel moments to produce an antiferromagnetic arrangement of orbital magnetic moments. Triangles with opposite orbital magnetization are related by $C_{4z}\mathcal{T}$ but not by \mathcal{PT} or $\tau\mathcal{T}$, consistent with general symmetry requirements for altermagnetism [1, 69, 70]. Based on the loop-current picture, we evaluate the magnetic multipole and find a nonzero magnetic octupole in the minimal model, which serves as a secondary order parameter in the Landau theory of d -wave altermagnetism [71] (see Supplementary Material (SM) for details [72]). Furthermore, we find that the current magnitude $|I|$ and direction are strongly phase-dependent: as shown in Fig. 1(f), $|I|$ varies as $\sin \phi$ due to time-reversal constraints, reversing direction upon $\phi \rightarrow -\phi$,

with a maximum magnitude at $\phi = \pm\pi/2$ and vanishing at $\phi = 0$ or $\pm\pi$, where the hopping becomes real. Finally, while loop currents provide a minimal realization with an intuitive physical picture in the present model, orbital altermagnetism is, in general, uniquely characterized by a symmetry-enforced alternating pattern of orbital magnetization and does not necessarily require a loop-current origin.

Before proceeding to real orbital altermagnetic materials, we make a few remarks on the general physics of orbital altermagnetism. (i) Orbital antiferromagnetism has been studied in interaction-driven loop-current states in correlated systems such as underdoped cuprates [73–78], SrRuO₃ [79], CeB₆ [80], and URu_{2-x}Fe_xSi₂ [81], but its realization as an *altermagnetic* order remains unexplored. (ii) Our proposed orbital altermagnetism is distinct from orbital order [51] and orbital-spin locking [82], where the staggered orbital ordering is leveraged to produce spin altermagnetism via breaking sublattice equivalence. (iii) Since orbital magnetization is often induced by effective complex hoppings via SOC or correlation effects, the symmetry must be described by magnetic groups rather than spin groups. Since symmetry required for orbital and spin altermagnetism is the same, they may coexist when orbital moments are aligned with spins or collectively shifted by a fraction of the period of the lattice. On the other hand, however, orbital altermagnetism may occur independent of spin ordering including spin altermagnetism when spins are absent or oriented differently, such as in ferromagnetic states.

Orbital altermagnetism in spin ferromagnets.— Strikingly, we find that orbital altermagnetism can exist in certain ferromagnets. Although the modern theory of orbital magnetization dictates that 2D systems lack in-plane orbital magnetic moments, the out-of-plane component M_z can adopt an alternating arrangement even in the absence of staggered spin order. From a symmetry perspective, altermagnetism requires the magnetic point group to belong to the first or third magnetic class (systems with $\tau\mathcal{T}$ symmetry are excluded here). Notably, several of these magnetic groups are compatible with in-plane spin ferromagnetism. In a 2D ferromagnet with in-plane spins and belonging to these classes, alternating M_z is allowed if the symmetry connects two sites with opposite M_z but excludes \mathcal{PT} and $C_{2z}\mathcal{T}$ symmetries. Only six magnetic point groups meet this criterion: 2 , m , m'_z , $2/m$, $m'_z m'_z 2'$, and $m' m'_z 2$.

In such *orbital-altermagnetic ferromagnets*, the role of spin alignment is merely to break time-reversal symmetry, while the alternating M_z pattern satisfies the magnetic point-group requirements. Two distinct cases arise: (1) Site-type orbital altermagnetism, where symmetry directly connects inequivalent atomic sites and reverses their M_z ; and (2) Loop-type orbital altermagnetism, where site symmetry forces $M_z = 0$ on all atomic sites, but the magnetic group permits circulating inter-site cur-

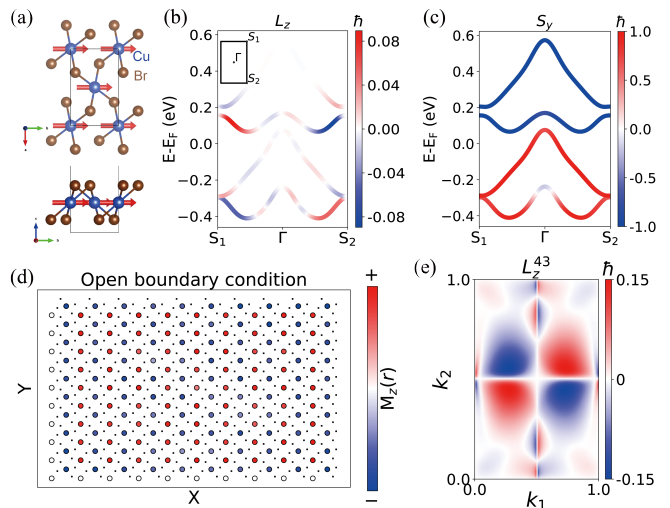


FIG. 2. (a) Top and side views of the monolayer CuBr₂. Spin magnetic moments localized on Cu atoms are annotated with red arrows. (b,c) Band structures of CuBr₂, with the color denoting the magnitude of L_z (b) and S_y (c) for each band. The inset displays the first Brillouin zone and high-symmetry points, with $S_1 = (0.5, 0.5)$ and $S_2 = (0.5, -0.5)$. (d) Real-space distribution of orbital magnetic moments in a 10×10 lattice under open boundary conditions at $\mu = 0$ eV. Red (blue) denotes positive (negative) $M_z(\mathbf{r})$. (e) Momentum-space distribution of $L_z(\mathbf{k})$ for the lowest conduction band (the 43rd band) across the Brillouin zone.

rents that generate staggered M_z located at empty plaquette centers.

A prototypical site-type example is CuBr₂ [83]. We consider an in-plane ferromagnetic configuration [Fig. 2(a)], where the Cu spins align ferromagnetically along y , giving the magnetic point group $2/m$. The two Cu atoms are related by either a glide mirror $\tilde{m}_y = \{m_y | \frac{1}{2}, \frac{1}{2}, 0\}$ or a glide rotation $\tilde{C}_{2y} = \{C_{2y} | \frac{1}{2}, \frac{1}{2}, 0\}$, both of which reverse M_z . Our first-principles calculations with SOC indeed reveal opposite-sign $M_z(\mathbf{r})$ on two Cu atoms in real space, as shown in Fig. 2(d). Furthermore, the band structure along the diagonal and antidiagonal \mathbf{k} -paths (S_1 - Γ - S_2) exhibits opposite L_z polarization with finite amplitude ($\sim 0.1\hbar$) [Fig. 2(b)], while maintaining persistent spin S_y polarization [Fig. 2(c)]. The \mathbf{k} -space distribution of $L_z(\mathbf{k})$ further manifests a defining characteristic d -wave pattern [see Fig. 2(e)]. Rotating the spins to the x axis changes the magnetic group to $2'/m'$, where the $\tilde{m}_y\mathcal{T}$ symmetry forces identical M_z on both Cu atoms, thereby suppressing orbital altermagnetism. Consequently, the presence or absence of orbital altermagnetism for different spin alignments produces distinct nonlinear orbital Edelstein effects to be used as an experimental signature of orbital altermagnetism (see SM [72]).

In addition to the above site-type orbital altermagnetism, we identify the honeycomb VS₂ monolayer [84] as a prototypical loop-type orbital altermagnetic ferromag-

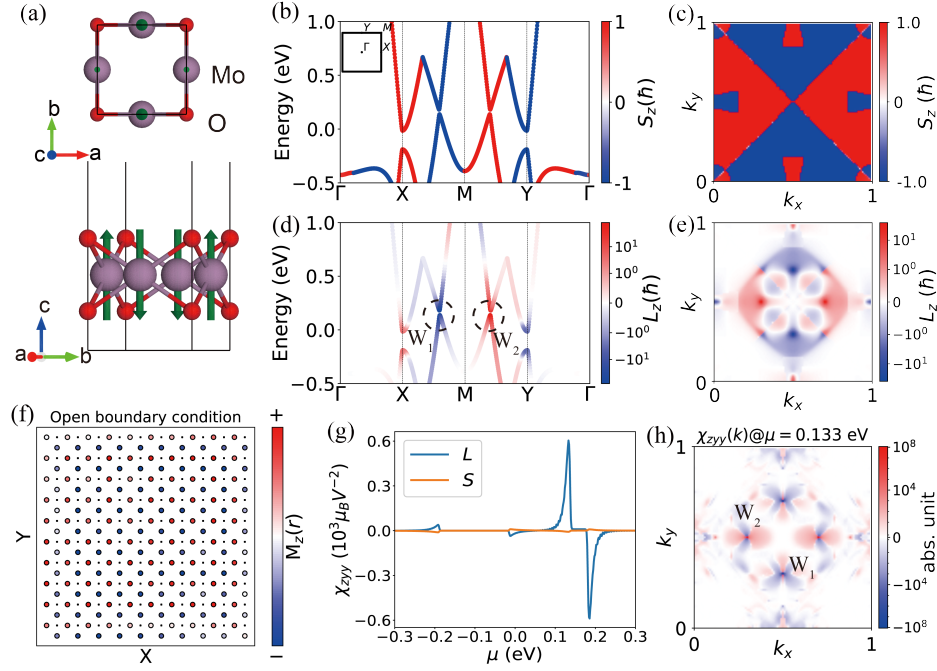


FIG. 3. (a) Top and side views of the monolayer MoO lattice. Green arrows indicate the spin magnetic moments on Mo atoms. (b) Spin- (S_z) and (d) Orbital- (L_z) resolved band structures, where nearly degenerated band crossing points at $\mu = 0.133$ eV are marked as W_1 and W_2 . The inset displays the Brillouin zone with high-symmetry points. (c,e) Momentum-space distribution of $S_z(\mathbf{k})$ (c) and $L_z(\mathbf{k})$ (e) for the highest valence band across the Brillouin zone, with k_x and k_y in reduced coordinates. Note that the color maps of $L_z(\mathbf{k})$ are presented in logarithmic scale for better visualization of its \mathbf{k} -space variation. (f) Real-space distribution of orbital magnetic moments in a 10×10 lattice under open boundary conditions at $\mu=0$ eV. Red (blue) denotes positive (negative) $M_z(\mathbf{r})$. (g) Nonlinear responses χ_{zyy}^X ($X = L$ or S) as a function of chemical potential μ from first-principles calculations. (h) Momentum-space distribution of $\chi_{zyy}(\mathbf{k})$ across the Brillouin zone at $\mu = 0.133$ eV.

net (see SM[72]). When the spins align along the a axis, the system belongs to the magnetic space group $2/m$, which forbids out-of-plane orbital magnetic moments at both V and S atomic sites. However, our calculations reveal two incoming currents of $0.44 \mu\text{A}$ and four outgoing currents of $0.22 \mu\text{A}$ on each V atom along the V-S bonds. These currents form closed loops within the V-S-V-S rhombi, circulating in opposite directions on adjacent plaquettes. This staggered loop-current pattern generates alternating out-of-plane orbital magnetic moments, thereby realizing orbital altermagnetism. The L_z -resolved band structure and the momentum-space distribution $L_z(\mathbf{k})$ (Fig. S5 in SM [72]) confirm the d -wave-like orbital-momentum locking, characteristic of orbital altermagnetism.

Orbital altermagnetism in conventional spin altermagnets.—We next illustrate the coexistence of spin and orbital altermagnetism using monolayer MoO as a representative example. The lattice structure [Fig. 3(a)] belongs to the $4'/mm'm$ magnetic point group. Its band structure exhibits clear momentum-dependent S_z and L_z polarizations, indicating simultaneous spin and orbital altermagnetic order [Fig. 3(b,d)]. The alternating momentum-space distribution of $L_z(\mathbf{k})$ for the highest valence band [Fig. 3(c,e)] and the staggered real-space

arrangement of orbital magnetic moments [Fig. 3(f)] confirm a d -wave-type orbital altermagnetism. Similar behavior is also found in monolayer CrO[85], with results presented in SM [72].

Like its spin counterpart, orbital altermagnetism contributes to a variety of magnetic phenomena, including the magneto-optical Kerr effect [86, 87], X-ray magnetic dichroism [88, 89], piezomagnetism [4, 22], and nonlinear Edelstein effect [90–92]. For instance, in the nonlinear Edelstein effect, a nonlinear current-induced spin or orbital magnetization can be expressed as $\delta X_a = \chi_{abc}^X E_b E_c$, where $a, b, c \in \{x, y, z\}$, E_a is the electric field, and $X = S$ or L denote the spin or orbital contributions, respectively. The nonlinear response tensor χ_{abc}^X is governed by band-geometric quantities such as the quantum metric, Berry curvature, and the matrix elements of spin or orbital angular momentum (see Sec. III SM for details [72]). In monolayer MoO, the combined symmetries $C_{4z}\mathcal{T}$ and $m_x\mathcal{T}$ strongly constrain the second-order response tensor χ_{zij}^X . For the out-of-plane response (z index), the time-reversal-even part is symmetry-forbidden, leaving only the intrinsic (time-reversal-odd) contribution. In this case, $m_x\mathcal{T}$ enforces $\chi_{zxy}^X = 0$, while $C_{4z}\mathcal{T}$ imposes $\chi_{zxx}^X = -\chi_{zyy}^X$. Consequently, for an in-plane electric field $\mathbf{E} = E(\sin\theta, \cos\theta)$, the induced out-of-plane

polarization varies as $\delta X_z \propto E^2 \cos 2\theta$, leading to a characteristic π -periodic angular dependence.

Remarkably, as shown in Fig. 3(e), the orbital contribution χ_{zzy}^L is substantially larger than its spin counterpart χ_{zzy}^S , indicating that the current-induced magnetization is dominated by orbital magnetization. A pronounced peak in χ_{zzy}^L occurs at $\mu = 0.133$ eV, originating from prominent orbital magnetic moments near the nearly degenerate band crossing points (W_1 and W_2) along the X - Γ and Y - Γ paths [see the bottom panel in Fig. 3(b)] [93, 94]. The \mathbf{k} -space distribution of $\chi_{zzy}^L(\mathbf{k})$ clearly shows that significant contributions are concentrated around the nearly degenerated points [Fig. 3(f) and Fig.S1 in SM [72]]. Since these points can be tuned close to the Fermi level via electric gating or tensile strain [95], we anticipate that a large nonlinear Edelstein response could be experimentally accessed through gating or strain, serving as a clear signature of orbital altermagnetism in monolayer MoO.

Discussion and summary—Recent studies have shown that weak orbital ferromagnetism or ferrimagnetism can emerge in altermagnets [3, 41, 96, 97] via SOC, arising from alternating g -tensor anisotropy or noncollinear magnetic moments. Such states are classified as M-type altermagnets [70, 98], which—in absence of SOC—exhibit perfect spin compensation, but develop a finite net magnetization from orbital magnetization and spin canting in the presence of SOC, and belong to ferromagnetic point groups. In contrast, our work reveals an inversed scenario: systems where orbital magnetic moments display a symmetry-protected altermagnetic order, yet the spin sector remains uncompensated (finite net spin). This concept naturally extends to spin ferrimagnets and noncollinear magnets belonging to ferromagnetic point groups. Moreover, the orbital altermagnetic state can, in principle, be tuned by spin reorientation (which changes the magnetic group symmetry) or by electric fields via orbital magnetoelectric coupling, offering new avenues for controlling altermagnetic responses.

Overall, our findings identify orbital altermagnetism as a broad and robust class of magnetic order—one that is distinct from, yet intertwined with, spin altermagnetism—opening a pathway to novel symmetry-driven magnetotransport phenomena and electrically tunable orbital-based spintronic devices. Experimentally, the significant orbital magnetization establishes giant current-induced orbital polarization as a transport signature of orbital altermagnetism and suggests that orbital degrees of freedom may play a dominant role in certain magnetic responses. We expect our theoretical proposal will stimulate immediate experimental interests, since recent experimental developments have made the detection of the real-space orbital magnetization patterns and altermagnetic orbital texture in momentum space possible, such as circular dichroism combined with soft x-ray angle-resolved photoemission spectroscopy [99], and

nitrogen-vacancy (NV)-center magnetometry [100] (see Sec. VII in SM [72] for detailed discussion). In addition to conventional magnetic materials studied here, the orbital altermagnetism is also expected to be achieved from the orbital antiferromagnetism in correlated systems, such as cuprates and cerium hexaboride CeB_6 , via various symmetry-engineering approaches such as strain [101], electric field [102–104], controllable stacking bilayers [105–108], ferroelectric substrate [109], and Januization [104, 110].

This work is supported by the National Key R&D Program of China (Grant No. 2021YFA1401600), and the National Natural Science Foundation of China (Grants No. 12074006 and 12474056). F.L. acknowledges support from DOE-BES (Grant No. DEFG02-04ER46148). The work was carried out at the National Supercomputer Center in Tianjin, and the calculations were performed on Tianhe new generation supercomputer. The high-performance computing platform of Peking University supported the computational resources.

Data availability—The data that support the findings of this article are openly available [111].

* Contact author: ftiger.liu@utah.edu

† Contact author: huaqing.huang@pku.edu.cn

- [1] L. Šmejkal, J. Sinova, and T. Jungwirth, Beyond conventional ferromagnetism and antiferromagnetism: A phase with nonrelativistic spin and crystal rotation symmetry, *Phys. Rev. X* **12**, 031042 (2022).
- [2] L. Šmejkal, J. Sinova, and T. Jungwirth, Emerging research landscape of altermagnetism, *Phys. Rev. X* **12**, 040501 (2022).
- [3] L. Šmejkal, R. González-Hernández, T. Jungwirth, and J. Sinova, Crystal time-reversal symmetry breaking and spontaneous hall effect in collinear antiferromagnets, *Sci. Adv.* **6**, eaaz8809 (2020).
- [4] H.-Y. Ma, M. Hu, N. Li, J. Liu, W. Yao, J.-F. Jia, and J. Liu, Multifunctional antiferromagnetic materials with giant piezomagnetism and noncollinear spin current, *Nat. Commun.* **12**, 2846 (2021).
- [5] C. Song, H. Bai, Z. Zhou, L. Han, H. Reichlova, J. H. Dil, J. Liu, X. Chen, and F. Pan, Altermagnets as a new class of functional materials, *Nat. Rev. Mater.* **10**, 473 (2025).
- [6] L. Bai, W. Feng, S. Liu, L. Šmejkal, Y. Mokrousov, and Y. Yao, Altermagnetism: Exploring new frontiers in magnetism and spintronics, *Adv. Funct. Mater.* **34**, 2409327 (2024).
- [7] L. Šmejkal, A. B. Hellenes, R. González-Hernández, J. Sinova, and T. Jungwirth, Giant and tunneling magnetoresistance in unconventional collinear antiferromagnets with nonrelativistic spin-momentum coupling, *Phys. Rev. X* **12**, 011028 (2022).
- [8] M. Naka, S. Hayami, H. Kusunose, Y. Yanagi, Y. Motome, and H. Seo, Spin current generation in organic antiferromagnets, *Nat. Commun.* **10**, 4305 (2019).
- [9] R. González-Hernández, L. Šmejkal, K. Vybírný, Y. Ya-

- hagi, J. Sinova, T. Jungwirth, and J. Železný, Efficient electrical spin splitter based on nonrelativistic collinear antiferromagnetism, *Phys. Rev. Lett.* **126**, 127701 (2021).
- [10] A. Bose, N. J. Schreiber, R. Jain, D.-F. Shao, H. P. Nair, J. Sun, X. S. Zhang, D. A. Müller, E. Y. Tsymlal, D. G. Schlom, and D. C. Ralph, Tilted spin current generated by the collinear antiferromagnet ruthenium dioxide, *Nat. Electron.* **5**, 267 (2022).
- [11] H. Bai, Y. C. Zhang, Y. J. Zhou, P. Chen, C. H. Wan, L. Han, W. X. Zhu, S. X. Liang, Y. C. Su, X. F. Han, F. Pan, and C. Song, Efficient spin-to-charge conversion via altermagnetic spin splitting effect in antiferromagnet RuO_2 , *Phys. Rev. Lett.* **130**, 216701 (2023).
- [12] Y. Fang, J. Cano, and S. A. A. Ghorashi, Quantum geometry induced nonlinear transport in altermagnets, *Phys. Rev. Lett.* **133**, 106701 (2024).
- [13] M. Ezawa, Third-order and fifth-order nonlinear spin-current generation in g -wave and i -wave altermagnets and perfectly nonreciprocal spin current in f -wave magnets, *Phys. Rev. B* **111**, 125420 (2025).
- [14] M. Naka, S. Hayami, H. Kusunose, Y. Yanagi, Y. Motome, and H. Seo, Spin current generation in organic antiferromagnets, *Nat. Commun.* **10**, 4305 (2019).
- [15] K. Tanaka, T. Nomoto, and R. Arita, Approaches to tunnel magnetoresistance effect with antiferromagnets, *J. Condens. Matter Phys.* **37**, 183003 (2025).
- [16] S. Bhowal and N. A. Spaldin, Ferroically ordered magnetic octupoles in d -wave altermagnets, *Phys. Rev. X* **14**, 011019 (2024).
- [17] J. Krempaský, L. Šmejkal, S. W. D'Souza, M. Hailaoui, G. Springholz, K. Uhlířová, F. Alarab, P. C. Constantinou, V. Strocov, D. Usanov, W. R. Pudelko, R. González-Hernández, A. Birk Hellenes, Z. Jansa, H. Reichlová, Z. Šobáň, R. D. Gonzalez Betancourt, P. Wadley, J. Sinova, D. Kriegner, J. Minár, J. H. Dil, and T. Jungwirth, Altermagnetic lifting of kramers spin degeneracy, *Nature* **626**, 517 (2024).
- [18] R. Takagi, R. Hirakida, Y. Settai, R. Oiwa, H. Takagi, A. Kitaori, K. Yamauchi, H. Inoue, J.-i. Yamaura, D. Nishio-Hamane, S. Itoh, S. Aji, H. Saito, T. Nakajima, T. Nomoto, R. Arita, and S. Seki, Spontaneous hall effect induced by collinear antiferromagnetic order at room temperature, *Nat. Mater.* **24**, 63 (2025).
- [19] H. Reichlova, R. Lopes Seeger, R. González-Hernández, I. Kounta, R. Schlitz, D. Kriegner, P. Ritzinger, M. Lammel, M. Leiviskä, A. Birk Hellenes, K. Olejník, V. Petříček, P. Doležal, L. Horak, E. Schmoranzero, A. Badura, S. Bertaina, A. Thomas, V. Baltz, L. Michez, J. Sinova, S. T. B. Goennenwein, T. Jungwirth, and L. Šmejkal, Observation of a spontaneous anomalous Hall response in the Mn_5Si_3 d -wave altermagnet candidate, *Nat. Commun.* **15**, 4961 (2024).
- [20] S. Lee, S. Lee, S. Jung, J. Jung, D. Kim, Y. Lee, B. Seok, J. Kim, B. G. Park, L. Šmejkal, C.-J. Kang, and C. Kim, Broken kramers degeneracy in altermagnetic MnTe , *Phys. Rev. Lett.* **132**, 036702 (2024).
- [21] M. Gu, Y. Liu, H. Zhu, K. Yananose, X. Chen, Y. Hu, A. Stroppa, and Q. Liu, Ferroelectric switchable altermagnetism, *Phys. Rev. Lett.* **134**, 106802 (2025).
- [22] M. Hu, X. Cheng, Z. Huang, and J. Liu, Catalog of c -paired spin-momentum locking in antiferromagnetic systems, *Phys. Rev. X* **15**, 021083 (2025).
- [23] L. Šmejkal, A. Marmodoro, K.-H. Ahn, R. González-Hernández, I. Turek, S. Mankovsky, H. Ebert, S. W. D'Souza, O. Šipr, J. Sinova, and T. Jungwirth, Chiral magnons in altermagnetic RuO_2 , *Phys. Rev. Lett.* **131**, 256703 (2023).
- [24] I. I. Mazin, K. Koepernik, M. D. Johannes, R. González-Hernández, and L. Šmejkal, Prediction of unconventional magnetism in doped FeSb_2 , *Proc. Natl. Acad. Sci. USA* **118**, e2108924118 (2021).
- [25] C. L. Tschirhart, M. Serlin, H. Polshyn, A. Shragai, Z. Xia, J. Zhu, Y. Zhang, K. Watanabe, T. Taniguchi, M. E. Huber, and A. F. Young, Imaging orbital ferromagnetism in a moiré chern insulator, *Science* **372**, 1323 (2021).
- [26] M. Serlin, C. L. Tschirhart, H. Polshyn, Y. Zhang, J. Zhu, K. Watanabe, T. Taniguchi, L. Balents, and A. F. Young, Intrinsic quantized anomalous hall effect in a moiré heterostructure, *Science* **367**, 900 (2020).
- [27] J.-X. Lin, Y.-H. Zhang, E. Morissette, Z. Wang, S. Liu, D. Rhodes, K. Watanabe, T. Taniguchi, J. Hone, and J. I. A. Li, Spin-orbit-driven ferromagnetism at half moiré filling in magic-angle twisted bilayer graphene, *Science* **375**, 437 (2022).
- [28] H. Polshyn, J. Zhu, M. A. Kumar, Y. Zhang, F. Yang, C. L. Tschirhart, M. Serlin, K. Watanabe, T. Taniguchi, A. H. MacDonald, and A. F. Young, Electrical switching of magnetic order in an orbital chern insulator, *Nature* **588**, 66 (2020).
- [29] A. L. Sharpe, E. J. Fox, A. W. Barnard, J. Finney, K. Watanabe, T. Taniguchi, M. A. Kastner, and D. Goldhaber-Gordon, Evidence of orbital ferromagnetism in twisted bilayer graphene aligned to hexagonal boron nitride, *Nano Lett.* **21**, 4299 (2021).
- [30] G. Chen, A. L. Sharpe, E. J. Fox, S. Wang, B. Lyu, L. Jiang, H. Li, K. Watanabe, T. Taniguchi, M. F. Crommie, M. A. Kastner, Z. Shi, D. Goldhaber-Gordon, Y. Zhang, and F. Wang, Tunable orbital ferromagnetism at noninteger filling of a moiré superlattice, *Nano Lett.* **22**, 238 (2022).
- [31] J. Xie, Z. Zhang, X. Chen, Y. H. Kwan, Z. Huo, J. Herzog-Arbeitman, L. Guo, K. Watanabe, T. Taniguchi, K. Liu, X. C. Xie, B. A. Bernevig, Z.-D. Song, and X. Lu, Unconventional orbital magnetism in graphene-based fractional chern insulators (2025), [arXiv:2506.01485](https://arxiv.org/abs/2506.01485) [cond-mat.mes-hall].
- [32] T. Han, Z. Lu, G. Scuri, J. Sung, J. Wang, T. Han, K. Watanabe, T. Taniguchi, L. Fu, H. Park, and L. Ju, Orbital multiferoicity in pentalayer rhombohedral graphene, *Nature* **623**, 41 (2023).
- [33] T. Han, Z. Lu, Y. Yao, J. Yang, J. Seo, C. Yoon, K. Watanabe, T. Taniguchi, L. Fu, F. Zhang, and L. Ju, Large quantum anomalous hall effect in spin-orbit proximitized rhombohedral graphene, *Science* **384**, 647 (2024).
- [34] J. Xie, Z. Huo, X. Lu, Z. Feng, Z. Zhang, W. Wang, Q. Yang, K. Watanabe, T. Taniguchi, K. Liu, Z. Song, X. C. Xie, J. Liu, and X. Lu, Tunable fractional chern insulators in rhombohedral graphene superlattices, *Nat. Mater.* **24**, 1042 (2025).
- [35] C. Huang, T. M. R. Wolf, W. Qin, N. Wei, I. V. Blinov, and A. H. MacDonald, Spin and orbital metallic magnetism in rhombohedral trilayer graphene, *Phys. Rev. B* **107**, L121405 (2023).
- [36] M. Das and C. Huang, Unconventional metallic ferromagnetism: Nonanalyticity and sign-changing behav-

- ior of orbital magnetization in rhombohedral trilayer graphene, *Phys. Rev. B* **109**, L060409 (2024).
- [37] X. Mu and J. Zhou, Valley-dependent giant orbital moments and transport features in rhombohedral graphene multilayers, *Phys. Rev. B* **111**, 165102 (2025).
- [38] L. M. Sandratskii and J. Kübler, Role of orbital polarization in weak ferromagnetism, *Phys. Rev. Lett.* **76**, 4963 (1996).
- [39] R. Shindou and N. Nagaosa, Orbital ferromagnetism and anomalous hall effect in antiferromagnets on the distorted fcc lattice, *Phys. Rev. Lett.* **87**, 116801 (2001).
- [40] N. Ito and K. Nomura, Anomalous hall effect and spontaneous orbital magnetization in antiferromagnetic weyl metal, *J. Phys. Soc. Jpn.* **86**, 063703 (2017).
- [41] D. Jo, D. Go, Y. Mokrousov, P. M. Oppeneer, S.-W. Cheong, and H.-W. Lee, Weak ferromagnetism in altermagnets from alternating g -tensor anisotropy, *Phys. Rev. Lett.* **134**, 196703 (2025).
- [42] A. Nersisyan and G. Vachnadze, Low-temperature thermodynamics of the two-dimensional orbital antiferromagnet, *J. Low Temp. Phys.* **77**, 293 (1989).
- [43] C. Varma, Mind the pseudogap, *Nature* **468**, 184 (2010).
- [44] C. M. Varma, Non-fermi-liquid states and pairing instability of a general model of copper oxide metals, *Phys. Rev. B* **55**, 14554 (1997).
- [45] C. M. Varma, Pseudogap phase and the quantum-critical point in copper-oxide metals, *Phys. Rev. Lett.* **83**, 3538 (1999).
- [46] C. M. Varma, Theory of the pseudogap state of the cuprates, *Phys. Rev. B* **73**, 155113 (2006).
- [47] A. Shekhter and C. M. Varma, Considerations on the symmetry of loop order in cuprates, *Phys. Rev. B* **80**, 214501 (2009).
- [48] C. M. Varma, Pseudogap in cuprates in the loop-current ordered state, *J. Phys. Condens. Matter* **26**, 505701 (2014).
- [49] S. Bulut, A. P. Kampf, and W. A. Atkinson, Instability towards staggered loop currents in the three-orbital model for cuprate superconductors, *Phys. Rev. B* **92**, 195140 (2015).
- [50] R. B. Laughlin, Fermi-liquid computation of the phase diagram of high- T_c cuprate superconductors with an orbital antiferromagnetic pseudogap, *Phys. Rev. Lett.* **112**, 017004 (2014).
- [51] V. Leeb, A. Mook, L. Šmejkal, and J. Knolle, Spontaneous formation of altermagnetism from orbital ordering, *Phys. Rev. Lett.* **132**, 236701 (2024).
- [52] Y. Yu, H. G. Suh, M. Roig, and D. F. Agterberg, Altermagnetism from coincident Van Hove singularities: application to κ -Cl, *Nat. Commun.* **16**, 2950 (2025).
- [53] J. a. A. Sobral, S. Mandal, and M. S. Scheurer, Fractionalized altermagnets: From neighboring and altermagnetic spin liquids to spin-symmetric band splitting, *Phys. Rev. Res.* **7**, 023152 (2025).
- [54] L. V. Pupim and M. S. Scheurer, Adatom engineering magnetic order in superconductors: Applications to altermagnetic superconductivity, *Phys. Rev. Lett.* **134**, 146001 (2025).
- [55] R. Siddharthan and A. Georges, Square kagome quantum antiferromagnet and the eight-vertex model, *Phys. Rev. B* **65**, 014417 (2001).
- [56] J. Richter, O. Derzhko, and J. Schulenburg, Magnetic-field induced spin-peierls instability in strongly frustrated quantum spin lattices, *Phys. Rev. Lett.* **93**, 107206 (2004).
- [57] A. W. Glaetzle, M. Dalmonte, R. Nath, I. Rousochatzakis, R. Moessner, and P. Zoller, Quantum spin-ice and dimer models with rydberg atoms, *Phys. Rev. X* **4**, 041037 (2014).
- [58] T. Thonhauser, D. Ceresoli, D. Vanderbilt, and R. Resta, Orbital magnetization in periodic insulators, *Phys. Rev. Lett.* **95**, 137205 (2005).
- [59] D. Ceresoli, T. Thonhauser, D. Vanderbilt, and R. Resta, Orbital magnetization in crystalline solids: Multi-band insulators, chern insulators, and metals, *Phys. Rev. B* **74**, 024408 (2006).
- [60] R. Resta, D. Ceresoli, T. Thonhauser, and D. Vanderbilt, Orbital magnetization in extended systems, *Chem. Phys. Chem.* **6**, 1815 (2005).
- [61] J. Shi, G. Vignale, D. Xiao, and Q. Niu, Quantum theory of orbital magnetization and its generalization to interacting systems, *Phys. Rev. Lett.* **99**, 197202 (2007).
- [62] R. Resta, Electrical polarization and orbital magnetization: the modern theories, *J. Phys.: Condens.Matter* **22**, 123201 (2010).
- [63] T. Thonhauser, Theory of orbital magnetization in solids, *Int. J. Mod. Phys. B* **25**, 1429 (2011).
- [64] D. Xiao, M.-C. Chang, and Q. Niu, Berry phase effects on electronic properties, *Rev. Mod. Phys.* **82**, 1959 (2010).
- [65] R. Bianco and R. Resta, Orbital magnetization as a local property, *Phys. Rev. Lett.* **110**, 087202 (2013).
- [66] A. Marrazzo and R. Resta, Locality of the anomalous hall conductivity, *Phys. Rev. B* **95**, 121114 (2017).
- [67] S.-S. Wang, Y. Yu, J.-H. Guan, Y.-M. Dai, H.-H. Wang, and Y.-Y. Zhang, Boundary effects on orbital magnetization for a bilayer system with different chern numbers, *Phys. Rev. B* **106**, 075136 (2022).
- [68] S. Bhowal and G. Vignale, Orbital Hall effect as an alternative to valley hall effect in gapped graphene, *Phys. Rev. B* **103**, 195309 (2021).
- [69] S. Zeng and Y.-J. Zhao, Description of two-dimensional altermagnetism: Categorization using spin group theory, *Phys. Rev. B* **110**, 054406 (2024).
- [70] S.-W. Cheong and F.-T. Huang, Altermagnetism classification, *npj Quantum Mater.* **10**, 38 (2025).
- [71] P. A. McClarty and J. G. Rau, Landau theory of altermagnetism, *Phys. Rev. Lett.* **132**, 176702 (2024).
- [72] See Supplemental Material at <http://link.aps.org/supplemental/xxx>, for more details about the expressions of orbital magnetization in reciprocal and real spaces, magnetic multipoles, the formula for nonlinear current-induced magnetization, detailed symmetry analysis of orbital altermagnetism, the first-principles calculation method, and more numerical result of material candidates, which includes Refs. [90–92, 95, 112–124].
- [73] M. E. Simon and C. M. Varma, Detection and implications of a time-reversal breaking state in underdoped cuprates, *Phys. Rev. Lett.* **89**, 247003 (2002).
- [74] S. Chakravarty, R. B. Laughlin, D. K. Morr, and C. Nayak, Hidden order in the cuprates, *Phys. Rev. B* **63**, 094503 (2001).
- [75] H. A. Mook, P. Dai, and F. Doğan, Observation of magnetic moments in the superconducting state of $\text{YBa}_2\text{Cu}_3\text{O}_{6.6}$, *Phys. Rev. B* **64**, 012502 (2001).
- [76] S. Chakravarty, H.-Y. Kee, and C. Nayak, Neutron scattering signature of d-density wave order in the cuprates,

- Int. J. Mod. Phys. B* **15**, 2901 (2001).
- [77] H.-Y. Kee and Y. B. Kim, Specific-heat anomaly in the d density wave state and emergence of inhomogeneous orbital antiferromagnetic order, *Phys. Rev. B* **66**, 012505 (2002).
- [78] V. I. Belyavsky, Y. V. Kopaev, and M. Y. Smirnov, Interplay of the superconducting state and orbital antiferromagnetic state of the high-temperature cuprate superconductors, *Phys. Rev. B* **72**, 132501 (2005).
- [79] D. F. Schroeter and S. Doniach, Orbital antiferromagnetism in coupled planar systems, *Phys. Rev. B* **69**, 094407 (2004).
- [80] F. J. Ohkawa, Orbital antiferromagnetism in CeB_6 , *J. Phys. Soc. Jpn.* **54**, 3909 (1985).
- [81] H.-H. Kung, S. Ran, N. Kanchanavatee, V. Krapivin, A. Lee, J. A. Mydosh, K. Haule, M. B. Maple, and G. Blumberg, Analogy between the “hidden order” and the orbital antiferromagnetism in $\text{URu}_{2-x}\text{Fe}_x\text{Si}_2$, *Phys. Rev. Lett.* **117**, 227601 (2016).
- [82] M. Vila, V. Sunko, and J. E. Moore, Orbital-spin locking and its optical signatures in altermagnets, *Phys. Rev. B* **112**, L020401 (2025).
- [83] L. Zhao, T.-L. Hung, C.-C. Li, Y.-Y. Chen, M.-K. Wu, R. K. Kremer, M. G. Banks, A. Simon, M.-H. Whangbo, C. Lee, J. S. Kim, I. Kim, and K. H. Kim, CuBr_2 – a new multiferroic material with high critical temperature, *Adv. Mater.* **24**, 2469 (2012).
- [84] Q. Ji, C. Li, J. Wang, J. Niu, Y. Gong, Z. Zhang, Q. Fang, Y. Zhang, J. Shi, L. Liao, X. Wu, L. Gu, Z. Liu, and Y. Zhang, Metallic vanadium disulfide nanosheets as a platform material for multifunctional electrode applications, *Nano Lett.* **17**, 4908 (2017).
- [85] P.-J. Guo, Z.-X. Liu, and Z.-Y. Lu, Quantum anomalous hall effect in collinear antiferromagnetism, *npj Comput. Mater.* **9**, 70 (2023).
- [86] S. Iguchi, H. Kobayashi, Y. Ikemoto, T. Furukawa, H. Itoh, S. Iwai, T. Moriwaki, and T. Sasaki, Magneto-optical spectra of an organic antiferromagnet as a candidate for an altermagnet, *Phys. Rev. Res.* **7**, 033026 (2025).
- [87] I. Gray, Q. Deng, Q. Tian, M. Chilcote, J. S. Dodge, M. Brahlek, and L. Wu, Time-resolved magneto-optical effects in the altermagnet candidate MnTe (2024), [arXiv:2404.05020 \[cond-mat.mtrl-sci\]](https://arxiv.org/abs/2404.05020).
- [88] A. Hariki, A. Dal Din, O. J. Amin, T. Yamaguchi, A. Badura, D. Kriegner, K. W. Edmonds, R. P. Campion, P. Wadley, D. Backes, L. S. I. Veiga, S. S. Dhesi, G. Springholz, L. Šmejkal, K. Výborný, T. Jungwirth, and J. Kuneš, X-ray magnetic circular dichroism in altermagnetic $\alpha\text{-MnTe}$, *Phys. Rev. Lett.* **132**, 176701 (2024).
- [89] W. Li, W. Li, M. Zou, Y. Yin, H. Li, G. Qu, Y. Huang, R. Yu, H. Yang, and B. Wang, Large anisotropic x-ray magnetic circular dichroism in altermagnetic CrSb with collinear antiferromagnetic structure at room temperature, *Phys. Rev. B* **111**, 224417 (2025).
- [90] C. Xiao, H. Liu, W. Wu, H. Wang, Q. Niu, and S. A. Yang, Intrinsic nonlinear electric spin generation in centrosymmetric magnets, *Phys. Rev. Lett.* **129**, 086602 (2022).
- [91] C. Xiao, W. Wu, H. Wang, Y.-X. Huang, X. Feng, H. Liu, G.-Y. Guo, Q. Niu, and S. A. Yang, Time-reversal-even nonlinear current induced spin polarization, *Phys. Rev. Lett.* **130**, 166302 (2023).
- [92] I. Baek, S. Han, S. Cheon, and H.-W. Lee, Nonlinear orbital and spin Edelstein effect in centrosymmetric metals, *npj Spintronics* **2**, 33 (2024).
- [93] M. Pan, H. Zeng, E. Wang, and H. Huang, Intrinsic orbital origin for the chirality-dependent nonlinear planar hall effect of topological nodal fermions in chiral crystals, *Phys. Rev. B* **111**, 075145 (2025).
- [94] Q. Yang, J. Xiao, I. Robredo, M. G. Vergniory, B. Yan, and C. Felser, Monopole-like orbital-momentum locking and the induced orbital transport in topological chiral semimetals, *Proc. Natl. Acad. Sci. USA* **120**, e2305541120 (2023).
- [95] B. Wu, Y.-l. Song, W.-x. Ji, P.-j. Wang, S.-f. Zhang, and C.-w. Zhang, Quantum anomalous hall effect in an antiferromagnetic monolayer of MoO , *Phys. Rev. B* **107**, 214419 (2023).
- [96] R. Bozorth and D. E. Walsh, Ferromagnetic moment of CoMnO_3 , *J. Phys. Chem. Solids* **5**, 299 (1958).
- [97] H. Koizumi, J.-i. Inoue, and H. Yanagihara, Magnetic anisotropy and orbital angular momentum in the orbital ferrimagnet cmnO_3 , *Phys. Rev. B* **100**, 224425 (2019).
- [98] S.-W. Cheong and F.-T. Huang, Altermagnetism with non-collinear spins, *npj Quantum Mater.* **9**, 13 (2024).
- [99] S. S. Brinkman, X. L. Tan, B. Brekke, A. C. Mathisen, O. Finnseth, R. J. Schenk, K. Hagiwara, M.-J. Huang, J. Buck, M. Kalläne, M. Hoesch, K. Rossnagel, K.-H. Ou Yang, M.-T. Lin, G.-J. Shu, Y.-J. Chen, C. Tusche, and H. Bentmann, Chirality-driven orbital angular momentum and circular dichroism in CoSi , *Phys. Rev. Lett.* **132**, 196402 (2024).
- [100] Y.-M. Xie and N. Nagaosa, Probing loop currents and collective modes of charge density waves in kagome materials with nv centers, *npj Quantum Materials* **10**, 64 (2025).
- [101] A. Chakraborty, R. González Hernández, L. Šmejkal, and J. Sinova, Strain-induced phase transition from antiferromagnet to altermagnet, *Phys. Rev. B* **109**, 144421 (2024).
- [102] P. Zhou, X. N. Peng, Y. Z. Hu, B. R. Pan, S. M. Liu, P. Lyu, and L. Z. Sun, Transition from antiferromagnetism to altermagnetism: symmetry breaking theory (2024), [arXiv:2410.17747 \[cond-mat.mtrl-sci\]](https://arxiv.org/abs/2410.17747).
- [103] I. Mazin, R. González-Hernández, and L. Šmejkal, Induced monolayer altermagnetism in $\text{mnp}(\text{s,se})_3$ and fese (2023), [arXiv:2309.02355 \[cond-mat.mes-hall\]](https://arxiv.org/abs/2309.02355).
- [104] H. Sun, P. Dong, C. Wu, and P. Li, Multifold induced antiferromagnet transformation into altermagnet and realized anomalous valley hall effect in two-dimensional materials (2025), [arXiv:2502.18024 \[cond-mat.mtrl-sci\]](https://arxiv.org/abs/2502.18024).
- [105] R. He, D. Wang, N. Luo, J. Zeng, K.-Q. Chen, and L.-M. Tang, Nonrelativistic spin-momentum coupling in antiferromagnetic twisted bilayers, *Phys. Rev. Lett.* **130**, 046401 (2023).
- [106] B. Pan, P. Zhou, P. Lyu, H. Xiao, X. Yang, and L. Sun, General stacking theory for altermagnetism in bilayer systems, *Phys. Rev. Lett.* **133**, 166701 (2024).
- [107] Y. Liu, J. Yu, and C.-C. Liu, Twisted magnetic van der waals bilayers: An ideal platform for altermagnetism, *Phys. Rev. Lett.* **133**, 206702 (2024).
- [108] S. Sheoran and S. Bhattacharya, Nonrelativistic spin splittings and altermagnetism in twisted bilayers of centrosymmetric antiferromagnets, *Phys. Rev. Mater.* **8**, L051401 (2024).
- [109] W. Sun, W. Wang, C. Yang, R. Hu, S. Yan, S. Huang,

- and Z. Cheng, Altermagnetism induced by sliding ferroelectricity via lattice symmetry-mediated magnetoelectric coupling, *Nano Lett.* **24**, 11179 (2024).
- [110] C. Liu, X. Li, X. Li, and J. Yang, Realizing abundant two-dimensional altermagnets with anisotropic spin current via spatial inversion symmetry breaking, *Nano Lett.* **25**, 9197 (2025).
- [111] M. Pan, F. Liu, and H. Huang, Data and scripts for 2d orbital altermagnetism, [10.5281/zenodo.17506196](https://zenodo.org/record/17506196) (2025).
- [112] A. Pezo, D. García Ovalle, and A. Manchon, Orbital hall effect in crystals: Interatomic versus intra-atomic contributions, *Phys. Rev. B* **106**, 104414 (2022).
- [113] S. Hayami and H. Kusunose, Unified description of electronic orderings and cross correlations by complete multipole representation, *J. Phys. Soc. Jpn.* **93**, 072001 (2024).
- [114] S. Hayami, M. Yatsushiro, Y. Yanagi, and H. Kusunose, Classification of atomic-scale multipoles under crystallographic point groups and application to linear response tensors, *Phys. Rev. B* **98**, 165110 (2018).
- [115] S. Hayami and H. Kusunose, Microscopic description of electric and magnetic toroidal multipoles in hybrid orbitals, *J. Phys. Soc. Jpn.* **87**, 033709 (2018).
- [116] M. Yatsushiro, H. Kusunose, and S. Hayami, Multipole classification in 122 magnetic point groups for unified understanding of multiferroic responses and transport phenomena, *Phys. Rev. B* **104**, 054412 (2021).
- [117] H. Kusunose, R. Oiwa, and S. Hayami, Symmetry-adapted modeling for molecules and crystals, *Phys. Rev. B* **107**, 195118 (2023).
- [118] J. P. Perdew, K. Burke, and M. Ernzerhof, Generalized Gradient Approximation Made Simple, *Phys. Rev. Lett.* **77**, 3865 (1996).
- [119] G. Kresse and J. Furthmüller, Efficiency of ab-initio total energy calculations for metals and semiconductors using a plane-wave basis set, *Comput. Mater. Sci.* **6**, 15 (1996).
- [120] X. Chen, D. Wang, L. Li, and B. Sanyal, Giant spin-splitting and tunable spin-momentum locked transport in room temperature collinear antiferromagnetic semimetallic cro monolayer, *Appl. Phys. Lett.* **123**, 022402 (2023).
- [121] C. E. Calderon, J. J. Plata, C. Toher, C. Oses, O. Levy, M. Fornari, A. Natan, M. J. Mehl, G. Hart, M. Buongiorno Nardelli, and S. Curtarolo, The aflow standard for high-throughput materials science calculations, *Comput. Mater. Sci.* **108**, 233 (2015).
- [122] A. A. Mostofi, J. R. Yates, Y.-S. Lee, I. Souza, D. Vanderbilt, and N. Marzari, wannier90: A tool for obtaining maximally-localised Wannier functions, *Comput. Phys. Commun.* **178**, 685 (2008).
- [123] Z. Xiao, J. Zhao, Y. Li, R. Shindou, and Z.-D. Song, Spin space groups: Full classification and applications, *Phys. Rev. X* **14**, 031037 (2024).
- [124] J. Etxebarria, J. M. Perez-Mato, E. S. Tasci, and L. Elcoro, Crystal tensor properties of magnetic materials with and without spin-orbit coupling. Application of spin point groups as approximate symmetries, *Acta Cryst. A* **81**, 317 (2025).
- [125] X. Qian, X.-B. Qiang, W. Zhu, Y. Huang, Y. Chen, H.-Z. Lu, Y. Ji, and K. Wang, Probing quantum geometric nonlinear magnetization via second-harmonic magneto-optical kerr effect, *Phys. Rev. B* **113**, L041407 (2026).
- [126] X.-B. Qiang, X. Liu, H.-Z. Lu, and X. C. Xie, Quantum christoffel nonlinear magnetization, *Phys. Rev. Lett.* **136**, 056302 (2026).
- [127] O. Busch, I. Mertig, and B. Göbel, Orbital hall effect and orbital edge states caused by s electrons, *Phys. Rev. Res.* **5**, 043052 (2023).
- [128] H. Watanabe, K. Shinohara, T. Nomoto, A. Togo, and R. Arita, Symmetry analysis with spin crystallographic groups: Disentangling effects free of spin-orbit coupling in emergent electromagnetism, *Phys. Rev. B* **109**, 094438 (2024).
- [129] H. Schiff, A. Corticelli, A. Guerreiro, J. Romhányi, and P. McClarty, The crystallographic spin point groups and their representations, *SciPost Phys.* **18**, 109 (2025).

Formula of Orbital Magnetization in Reciprocal and Real Spaces

Orbital magnetism arises from the motion of electrons in atomic orbitals or Bloch states and plays a crucial role in diverse magnetic and transport phenomena, particularly in systems where spin contributions are suppressed or symmetry-forbidden. Unlike spin magnetic moments—typically described by exchange interactions or Zeeman coupling—orbital magnetic moments originate from the circulation of charge in real or momentum space and are intrinsically tied to the geometric and topological properties of electronic wavefunctions.

From a theoretical standpoint, the orbital magnetic moment of a Bloch electron in band n at wavevector \mathbf{k} can be expressed as the expectation value of the self-rotation of a wave packet about its center of mass. This is formalized in the modern theory of orbital magnetization, which extends semiclassical concepts into a gauge-invariant quantum framework. In two dimensions, only the out-of-plane component is well defined. At zero temperature in a two-

dimensional (2D) periodic crystal, the total orbital magnetization is given by [58–60, 67]:

$$\begin{aligned}
M &= M_{\text{LC}} + M_{\text{IC}} + M_{\text{BC}}, \\
M_{\text{LC}} &= \frac{e}{2\hbar c} \text{Im} \sum_n \int_{\epsilon_{n\mathbf{k}} \leq \mu} [d\mathbf{k}] \langle \partial_{\mathbf{k}} u_{n\mathbf{k}} | \times H_{\mathbf{k}} | \partial_{\mathbf{k}} u_{n\mathbf{k}} \rangle, \\
M_{\text{IC}} &= \frac{e}{2\hbar c} \text{Im} \sum_n \int_{\epsilon_{n\mathbf{k}} \leq \mu} [d\mathbf{k}] \epsilon_{n\mathbf{k}} \langle \partial_{\mathbf{k}} u_{n\mathbf{k}} | \times | \partial_{\mathbf{k}} u_{n\mathbf{k}} \rangle, \\
M_{\text{BC}} &= -\mu \frac{e}{2\pi\hbar c} \mathcal{C}, \\
\mathcal{C} &= \frac{1}{2\pi} \text{Im} \sum_n \int_{\epsilon_{n\mathbf{k}} \leq \mu} d\mathbf{k} \langle \partial_{\mathbf{k}} u_{n\mathbf{k}} | \times | \partial_{\mathbf{k}} u_{n\mathbf{k}} \rangle,
\end{aligned} \tag{2}$$

where $|u_{n\mathbf{k}}\rangle$ is the cell-periodic Bloch function and $\epsilon_{n\mathbf{k}}$ the band energy. All summations in Eq. (2) are over occupied bands n up to μ . Here, M_{LC} corresponds to the local circulation (LC) of Wannier orbitals, M_{IC} arises from the itinerant circulation (IC) of Bloch electrons, and M_{BC} is a topological contribution proportional to the Chern number \mathcal{C} (quantized when μ is in the bulk gap), which is finite only in systems with broken time-reversal symmetry and nontrivial topology.

To resolve orbital-momentum locking in momentum space for 2D systems with trivial topology ($\mathcal{C} = 0$), we employ the band- and \mathbf{k} -resolved expression of the orbital magnetic moment [59, 62–64],

$$M_{n\mathbf{k}} = \frac{e}{2\hbar c} \text{Im} \langle \partial_{\mathbf{k}} u_{n\mathbf{k}} | \times (H_{\mathbf{k}} - \epsilon_{n\mathbf{k}}) | \partial_{\mathbf{k}} u_{n\mathbf{k}} \rangle, \tag{3}$$

More specifically,

$$M_{n\mathbf{k}} = -\frac{e}{2\hbar c} \text{Im} \sum_{m \neq n} \frac{\langle u_{n\mathbf{k}} | \hat{\mathbf{v}} | u_{m\mathbf{k}} \rangle \times \langle u_{m\mathbf{k}} | \hat{\mathbf{v}} | u_{n\mathbf{k}} \rangle}{\epsilon_{n\mathbf{k}} - \epsilon_{m\mathbf{k}}}, \tag{4}$$

where $\hat{\mathbf{v}} = \frac{1}{\hbar} \nabla_{\mathbf{k}} H(\mathbf{k})$ is the velocity operator. From this expression, the orbital magnetic moment is expected to increase significantly in regions where the bands are nearly degenerate. In two dimensions, $M_{n\mathbf{k}}$ is along the out-of-plane direction and is directly related to the orbital angular momentum via

$$M_{n\mathbf{k}} = -g_L \mu_B L_z(\mathbf{k}), \tag{5}$$

where μ_B is the Bohr magneton and $g_L = 1$ the Landé g-factor [68].

To characterize orbital magnetization in systems lacking full translational symmetry (e.g., under open boundary conditions or disorder), a real-space formulation is often more appropriate. Analogous to the above \mathbf{k} -space integration, orbital magnetization and its constituent terms can also be expressed as a real-space integration $M = \frac{1}{A} \int_A d\mathbf{r} m(\mathbf{r})$, which has the form of a real-space average over some region with an area A . Following Refs. [65–67], the corresponding orbital magnetization density $m(\mathbf{r})$ can be written as a sum of gauge-invariant local markers:

$$\begin{aligned}
m(\mathbf{r}) &= m_{\text{LC}}(\mathbf{r}) + m_{\text{IC}}(\mathbf{r}) + m_{\text{BC}}(\mathbf{r}), \\
m_{\text{LC}}(\mathbf{r}) &= \frac{e}{\hbar c} \text{Im} \langle \mathbf{r} | P x Q H Q y P | \mathbf{r} \rangle, \\
m_{\text{IC}}(\mathbf{r}) &= -\frac{e}{\hbar c} \text{Im} \langle \mathbf{r} | Q x P H P y Q | \mathbf{r} \rangle, \\
m_{\text{BC}}(\mathbf{r}) &= -\mu \frac{2e}{\hbar c} \text{Im} \langle \mathbf{r} | Q x P y Q | \mathbf{r} \rangle,
\end{aligned} \tag{6}$$

where P is the ground-state projector and $Q = 1 - P$ its complement:

$$P = \sum_{\epsilon_i \leq \mu} |\varphi_i\rangle \langle \varphi_i|, \quad H|\varphi_i\rangle = \epsilon_i |\varphi_i\rangle. \tag{7}$$

This formalism provides a position-resolved, gauge-invariant description of orbital magnetization, enabling direct evaluation of orbital textures in both tight-binding and first-principles frameworks.

In the main text, we apply this approach to the minimal tight-binding model of orbital altermagnetism. The resulting real-space orbital magnetization $m(\mathbf{r})$, computed from Eq. (6), serves as a key diagnostic for identifying staggered orbital ordering patterns in real space.

Magnetic octupole and Magnetic Toroidal quadrupole

In both theoretical models and real magnetic materials, orbital magnetic moments can often be interpreted as arising from local loop currents. Accordingly, the magnetic (M) multipoles and magnetic toroidal (MT) multipoles are defined from the explicit current distribution. Previous studies [113] have established that imaginary hopping in tight-binding models corresponds to MT multipoles, thereby linking orbital magnetism intrinsically to these multipoles.

Magnetic multipoles M_{lm} and magnetic toroidal multipoles T_{lm} exhibit distinct transformation properties under spatial inversion \mathcal{P} and time-reversal symmetry \mathcal{T} [114]:

$$M_{lm} \xrightarrow{(\mathcal{P}, \mathcal{T})} [(-1)^{l+1}, -1], \quad T_{lm} \xrightarrow{(\mathcal{P}, \mathcal{T})} [(-1)^l, -1].$$

From these transformation rules, it follows that collinear altermagnets can uniquely host MT quadrupoles or M octupoles, which are absent in conventional ferromagnets or antiferromagnets.

The explicit definitions are given as [115]:

$$M_{lm} = \frac{1}{c(l+1)} \int dr [\mathbf{r} \times \mathbf{j}_e(\mathbf{r})] \cdot \nabla O_{lm}(\mathbf{r}), \quad (8)$$

$$T_{lm} = \frac{1}{c(l+1)} \int dr [\mathbf{r} \cdot \mathbf{j}_e(\mathbf{r})] O_{lm}(\mathbf{r}), \quad (9)$$

where $\mathbf{j}_e(\mathbf{r})$ is the electric current density, and

$$O_{lm}(\mathbf{r}) = \sqrt{\frac{4\pi}{2l+1}} r^l Y_{lm}^*(\hat{\mathbf{r}})$$

is expressed in terms of the spherical harmonics $Y_{lm}(\hat{\mathbf{r}})$, with l and m denoting the azimuthal and magnetic quantum numbers, respectively.

For the minimal model defined in Eq. (1) in the main text, we reveal that $T_{xy} \neq 0$ and $M_z^\beta \neq 0$ (with $O_z^\beta = \frac{\sqrt{15}}{2} z(x^2 - y^2)$), consistent with the allowed multipoles of the corresponding magnetic point group [116]. Particularly, the nonzero magnetic octupole M_z^β can serve as a secondary order parameter in the Landau theory of the d -wave altermagnetism [71]. The nonzero T_{xy} can also be directly traced back to the imaginary hopping terms in the tight-binding model. By evaluating the symmetry-adapted multipole basis (SAMB) for the bond cluster [117], we find that in the D_{4h} point group, only the irreducible representation B_{2g} yields a non-zero toroidal quadrupole, which precisely corresponds to T_{xy} .

Intrinsic nonlinear current-induced spin and orbital magnetization

In this section, we provide a brief introduction to the formalism of the intrinsic nonlinear Edelstein effect. For a 2D system with either C_{2z} or \mathcal{P} symmetry, the linear spin and orbital responses are forbidden by symmetry. In such cases, the leading contribution arises at the second order:

$$\delta X_a = \chi_{abc}^X E_b E_c, \quad (10)$$

where X_a denotes the a -th component of either the orbital angular momentum L_a or the spin angular momentum S_a . The nonlinear response tensor χ_{abc} can be decomposed according to its parity under time-reversal symmetry [90–92, 125, 126]:

$$\begin{aligned} \chi_{abc}^{\text{even}} &= \tau \sum_n \int [d\mathbf{k}] f_0 \partial_c \gamma_{ab}^{X,n}, \\ \chi_{abc}^{\text{odd}} &= \frac{1}{2} \int [d\mathbf{k}] \sum_n \left[\Lambda_{abc,n}^X f_0 - (X_{a,n} G_{bc,n} - v_{b,n} \mathcal{G}_{ac,n}^X - v_{c,n} \mathcal{G}_{ab,n}^X) f_0' \right]. \end{aligned} \quad (11)$$

Here $[d\mathbf{k}] \equiv d\mathbf{k}/(2\pi)^d$ is a shorthand notation for integration over the Brillouin zone in d dimensions, and f_0 is the Fermi-Dirac distribution with unperturbed band energy ϵ_n , and f_0' is its derivative. The quantity $X_{a,n} = \langle u_n | \hat{X}_a | u_n \rangle$

is the intraband matrix element of spin or orbital angular momentum, and $v_{a,n}$ is the intraband velocity matrix element.

The Zeeman-like field \mathbf{h} couples to the spin or orbital degree of freedom in the form of $-\hat{\mathbf{s}} \cdot \mathbf{h}$ or $-\hat{\mathbf{L}} \cdot \mathbf{h}$. Therefore, in the presence of an external field, one can define the Berry connection and the related quantities in the h -space [90]. For example, the h -space Berry connection is defined as $\mathfrak{A}_i = \langle u_n(\mathbf{k}) | i\partial_{h_i} | u_n(\mathbf{k}) \rangle$. The Berry connection polarizability (BCP) and the h -space BCP are defined as

$$\begin{aligned} G_{ab,n} &= 2\text{Re} \sum_{m \neq n} \frac{v_{a,nm} v_{b,mn}}{(\epsilon_n - \epsilon_m)^3}, \\ \mathcal{G}_{ab,n}^S &= -2\text{Re} \sum_{m \neq n} \frac{s_{a,nm} v_{b,mn}}{(\epsilon_n - \epsilon_m)^3}, \\ \mathcal{G}_{ab,n}^O &= -2\text{Re} \sum_{m \neq n} \frac{M_{a,nm} v_{b,mn}}{(\epsilon_n - \epsilon_m)^3}, \end{aligned} \quad (12)$$

where the numerator involves the interband matrix elements of spin and velocity operators, $s_{a,nm}$ and $v_{a,nm}$, $M_{mn} = \sum_{l \neq n} (v_{ml} + \delta_{lm} v_{nn}) \times A_{ln}/2$ is the interband orbital magnetic moment, $A_{mn} = \langle u_m | i\partial_{\mathbf{k}} | u_n \rangle$ is the Berry connection. The anomalous spin polarizability (ASP) and the anomalous orbital polarizability (AOP) is given by

$$\begin{aligned} \gamma_{ab}^{S,n}(\mathbf{k}) &= 2g\mu_B \text{Im} \sum_{m \neq n} \frac{s_{a,nm} v_{b,mn}}{(\epsilon_n - \epsilon_m)^2}, \\ \gamma_{ab}^{L,n}(\mathbf{k}) &= -2\text{Im} \sum_{m \neq n} \frac{M_{a,nm} v_{b,mn}}{(\epsilon_n - \epsilon_m)^2} - \frac{e}{2\hbar} \epsilon_{akl} \Gamma_n^{lkb}, \end{aligned} \quad (13)$$

where the quantum Christoffel symbol is defined as

$$\begin{aligned} \Gamma_n^{abc} &= \frac{1}{2} (\partial_c g_n^{ba} + \partial_b g_n^{ac} - \partial_a g_n^{bc}), \\ g_n^{ab} &= \text{Re} \sum_{m \neq n} A_{nm}^i A_{mn}^j. \end{aligned} \quad (14)$$

The second-order response kernel $\Lambda_{abc,n}^X$ is given by

$$\begin{aligned} \Lambda_{abc,n}^X &= -2\text{Re} \sum_{m \neq n} \left[\frac{3v_{b,nm} v_{c,mn} (X_{a,nn} - X_{a,mm})}{(\epsilon_n - \epsilon_m)^4} - \frac{(\partial_b X_a)_{nm} v_{c,mn} + (\partial_c X_a)_{nm} v_{b,mn}}{(\epsilon_n - \epsilon_m)^3} \right. \\ &\quad \left. - \sum_{l \neq n} \frac{(v_{b,lm} v_{c,mn} + v_{c,lm} v_{b,mn}) X_{a,nl}}{(\epsilon_n - \epsilon_l)(\epsilon_n - \epsilon_m)^3} - \sum_{l \neq m} \frac{(v_{b,ln} v_{c,nm} + v_{c,ln} v_{b,nm}) X_{a,ml}}{(\epsilon_m - \epsilon_l)(\epsilon_n - \epsilon_m)^3} \right]. \end{aligned} \quad (15)$$

Finally, the orbital angular momentum (OAM) matrix elements follow from the modern theory of orbital magnetization [112]:

$$\langle u_n | \hat{\mathbf{L}} | u_m \rangle = i \frac{e\hbar^2}{4g_L \mu_B} \sum_{q \neq n,m} \left(\frac{1}{\epsilon_q - \epsilon_n} + \frac{1}{\epsilon_q - \epsilon_m} \right) \cdot \langle u_n | \hat{\mathbf{v}} | u_q \rangle \times \langle u_q | \hat{\mathbf{v}} | u_m \rangle. \quad (16)$$

The diagonal element of the orbital angular momentum \mathbf{L}_n is linearly related to the orbital magnetization. In 2D systems, its z-component corresponds to the out-of-plane component of the orbital magnetic moment via Eq. (5) [68].

Note that the matrix elements of the orbital angular momentum (OAM) here are different from those of the atom-centered approximation (ACA), which assumes that the OAM originates from the region centered on the atomic sites. Within ACA, $\hat{\mathbf{L}}$ reduces to the on-site atomic orbital angular momentum operator that mixes orbitals located at the same lattice site [112, 127]. While the ACA is often adequate for wide-gap semiconductors, it is known to fail in both narrow-gap systems and in transition metals.

Symmetry Analysis of Orbital Altermagnetism in Two Dimensions

Definition and symmetry constraints of 2D orbital altermagnetism

We define a 2D orbital altermagnet as a system whose real space can be partitioned into two sublattices carrying nonzero but opposite orbital magnetic moments. The sublattices may consist either of atomic sites or of loop currents on bonds. In both cases, we focus on the out-of-plane component $M_z(\mathbf{r})$, which is the natural component in a two-dimensional geometry.

A key feature of orbital altermagnetism is that the net out-of-plane orbital magnetization vanishes, which the local distribution is not identically zero. This is the orbital analogue of a compensated antiferromagnetic-like or altermagnetic-like pattern, with the magnetic degree of freedom originating from orbital motion rather than from spin.

In momentum space, for an orbital altermagnet, the momentum-resolved orbital magnetic moment or the orbital angular momentum $L_z(\mathbf{k})$ must not be forced to vanish by symmetry across the Brillouin zone. In particular, any antiunitary symmetry that maps $\mathbf{k} \rightarrow \mathbf{k}$ while flipping the sign of the axial out-of-plane moment would enforce $L_z(\mathbf{k}) = 0$, and is therefore incompatible with a finite orbital moment texture. This includes, for example, \mathcal{PT} or $C_{2z}\mathcal{T}$.

Screening magnetic point groups compatible with 2D orbital altermagnetism

We performed an exhaustive symmetry screening over all magnetic point groups to identify those that can host 2D orbital altermagnetism. The screening procedure follows directly from the definition and the symmetry constraints discussed above.

(i) *Remark on gray magnetic point groups and the underlying MSG type.* A gray (type-II) magnetic point group contains the pure time-reversal operation \mathcal{T} at the point-group level. Importantly, the *same* gray point group can originate from two physically different situations at the magnetic space-group (MSG) level: a type-II (gray) MSG, where \mathcal{T} appears as $\{1|\mathbf{0}\}\mathcal{T}$ and the crystal is nonmagnetic; or a type-IV MSG, where the relevant antiunitary symmetry is a *generalized* time reversal of the form

$$\tilde{\mathcal{T}} = \{1|\boldsymbol{\tau}\}\mathcal{T}, \quad (17)$$

with a nontrivial translation $\boldsymbol{\tau}$, which projects to \mathcal{T} in the point-group description.

Since the definition of 2D orbital altermagnetism concerns magnetic states with a nontrivial local orbital-moment pattern, we do *not* consider the nonmagnetic realization (type-II MSG) of gray point groups. Therefore, throughout the screening below, whenever a gray (type-II) magnetic point group is encountered, it is implicitly understood as the realization compatible with a type-IV MSG (i.e., with $\tilde{\mathcal{T}} = \{1|\boldsymbol{\tau}\}\mathcal{T}$ rather than $\{1|\mathbf{0}\}\mathcal{T}$).

(ii) *Only operations preserving the $k_z = 0$ plane.* Since we target a two-dimensional orbital texture characterized on the $k_z = 0$ plane, we only keep symmetry operations that leave this plane invariant. Concretely, we consider the subgroup of operations g such that

$$g : (k_x, k_y, 0) \mapsto (k'_x, k'_y, 0). \quad (18)$$

Operations that mix k_z with in-plane components are discarded for the purpose of the 2D classification.

(iii) *Existence of a symmetry that flips the out-of-plane orbital moment.* To realize the defining compensated pattern (zero net out-of-plane moment but nonzero local M_z), the symmetry group must contain at least one operation that maps the two sublattices onto each other while reversing the sign of the out-of-plane axial moment. In other words, we require the presence of a symmetry element g such that

$$M_z(\mathbf{r}) \xrightarrow{g} -M_z(g\mathbf{r}), \quad (19)$$

which guarantees cancellation of the net z -component upon summation over the symmetry-related sublattices (or loop-current substructures), while still allowing $M_z(\mathbf{r}) \neq 0$.

(iv) *Exclusion of symmetries that force $L_z(\mathbf{k})$ to vanish.* Finally, we exclude magnetic point groups containing any (antiunitary) operation that enforces the constraint

$$L_z(\mathbf{k}) = -L_z(\mathbf{k}), \quad (20)$$

which would symmetry-force $L_z(\mathbf{k}) \equiv 0$ on the $k_z = 0$ plane and thus forbid a finite orbital texture. In practice, this removes cases where an antiunitary symmetry maps $\mathbf{k} \rightarrow \mathbf{k}$ while flipping the sign of the axial out-of-plane moment (for example, \mathcal{PT} or $C_{2z}\mathcal{T}$, as discussed above).

(v) *Conventions and coordinate choices.* Throughout this work, symmetry operations are taken in their standard settings with conventional axis orientations. For a given material, the crystallographic axes may be rotated relative to these standard conventions, and a corresponding change of coordinates may be required to apply the screening rules to a specific structure. Such material-dependent axis redefinitions do not change the symmetry logic, but they can affect which component is identified as the out-of-plane direction in the chosen coordinate system. A case-by-case coordinate alignment is therefore left for future, system-specific analyses and is not pursued in detail here. For example, consider the magnetic point group $m'm2'$. In the standard convention one may represent its generators as $m_x\mathcal{T}$, m_y , and $C_{2z}\mathcal{T}$; in this orientation $C_{2z}\mathcal{T}$ can map $\mathbf{k} \rightarrow \mathbf{k}$ while reversing the axial out-of-plane moment, thereby symmetry-forcing $L_z(\mathbf{k})$ to vanish and excluding 2D orbital altermagnetism. However, under a different (rotated) axis assignment for the same abstract group, one may instead take $m_z\mathcal{T}$, m_x , and C_{2y} as generators; in that coordinate choice, the corresponding constraints no longer forbid a finite $L_z(\mathbf{k})$ texture, and 2D orbital altermagnetism becomes symmetry-allowed.

Applying the above criteria yields a restricted set of magnetic point groups compatible with two-dimensional orbital altermagnetism, which we summarize in Table I and discuss below.

TABLE I. Magnetic point groups (MPGs) that allow 2D orbital altermagnetism, together with the symmetry-enforced leading splitting wave of the orbital texture. The classification is given in the standard setting with conventional axis orientations; for a specific material, an appropriate rotation of the coordinate axes may be required.

Leading wave	Allowed magnetic point groups (MPGs)
<i>p</i> -wave	1.1', 2.1, 2.1', m.1, m.1'
<i>d</i> -wave	2/m.1, 222.1, mm2.1, mmm.1, 4', -4', 4'/m, 4'22', 4'm'm, -4'2'm, -4'2m', 4'/mm'm
<i>g</i> -wave	422.1, 4mm.1, -42m.1, 4/mmm,
<i>f</i> -wave	3.1', 32.1, 32.1', 3m.1, 3m.1', -6.1', -6', -6m2.1, -6m2.1', -6'm'2, -6'm2'
<i>i</i> -wave	-3m.1, 622.1, 6mm.1, 6/mmm.1,

Magnetic point groups allowing the 2D orbital-altermagnetic ferromagnet

To identify the magnetic point groups that permit 2D orbital altermagnetic ferromagnets, we impose the following criteria: (i) the group must be compatible with ferromagnetism; (ii) it must contain at least one symmetry operation that reverses the z -component of magnetization (see Fig. 4); (iii) both \mathcal{PT} and $C_{2z}\mathcal{T}$ symmetries must be excluded. Applying these screening criteria yields only six compatible magnetic point groups: 2 , m , m'_z , $2/m$, $m'_z m2'$, and $m' m'_z 2$. Among these, only the $2/m$ group exhibits even-parity altermagnetism, which is invariant under $\mathbf{k} \rightarrow -\mathbf{k}$ (see Table II).

TABLE II. Magnetic point groups allowing 2D orbital altermagnetic ferromagnets. The criteria are: (i) compatibility with ferromagnetism, (ii) presence of at least one operation reversing the z -component of magnetization, and (iii) exclusion of both \mathcal{PT} and $C_{2z}\mathcal{T}$ symmetries. The parity column indicates the parity under inversion $\mathbf{k} \rightarrow -\mathbf{k}$.

Magnetic point group	Representative operations	Parity
2	C_{2y}	Odd
m	m_x	Odd
m'_z	$m_z\mathcal{T}$	Odd
$2/m$	C_{2x}, m_x	Even
$m'_z m2'$	$m_z\mathcal{T}, m_x, C_{2y}\mathcal{T}$	Odd
$m' m'_z 2$	$m_x\mathcal{T}, m_z\mathcal{T}, C_{2y}$	Odd

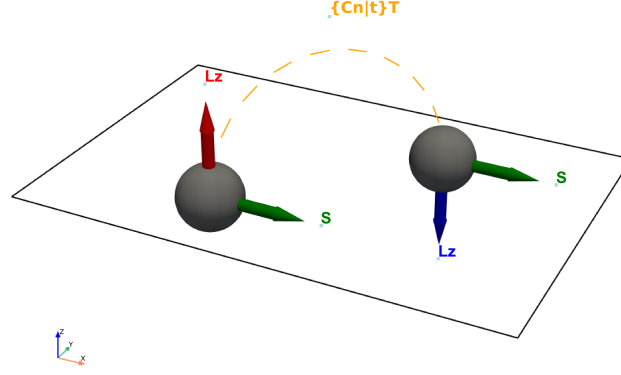


FIG. 4. A schematic diagram illustrates how an in-plane ferromagnet can be used to achieve an out-of-plane orbital antiferromagnet. A combined $\{C_n|t\}\mathcal{T}$ symmetry links to sites with opposite orbital angular momentum while maintaining the in-plane spin. Here, the arrangement of other non-magnetic elements is omitted, though they are typically required for the breaking of the \mathcal{PT} or $\tau\mathcal{T}$ symmetry.

Role of spin-orbit coupling in 2D orbital altermagnetism

We emphasize that spin-orbit coupling (SOC) is central for the two-dimensional setting considered in this work. In the absence of SOC, spin and orbital sectors are decoupled. As a result, symmetry operations acting in spin space influence the orbital magnetic moment only through whether the associated symmetry is unitary or antiunitary when projected onto the orbital sector. In particular, for collinear or coplanar magnetic configurations, one can define an *effective orbital time-reversal-like* antiunitary symmetry, which enforces the local orbital moment in real space to vanish identically. Therefore, such SOC-free collinear/coplanar states do not satisfy our definition of orbital altermagnetism, which requires $M_{\text{orb}}(\mathbf{r}) \neq 0$.

More specifically, the real-space orbital magnetic moment $M_{\text{orb}}(\mathbf{r})$ (an axial vector) transforms under a general spin space-group operation $\{W|R|\mathbf{t}\}$ as

$$M_{\text{orb}}(\mathbf{r}) = \det(W) \det(R) R \cdot M_{\text{orb}}(\{R|\mathbf{t}\}^{-1}\mathbf{r}), \quad (21)$$

where $\det(W) = -1$ can be viewed as an effective orbital time-reversal symmetry, R is a proper or improper rotation, and \mathbf{t} is a translation. Equation (21) implies that if the symmetry group contains an antiunitary operation of the form $\{W|1|\mathbf{0}\}$ with $\det(W) = -1$ that leaves \mathbf{r} invariant, then

$$M_{\text{orb}}(\mathbf{r}) = -M_{\text{orb}}(\mathbf{r}) = 0, \quad (22)$$

so the local orbital moment is symmetry-forced to vanish everywhere. Such operations can be viewed as an “orbital time-reversal” symmetry in the SOC-free limit [128].

For collinear magnetic configurations with spins aligned along the z axis, the effective orbital time-reversal symmetry can be written as $\{\mathcal{T}U_{xy}(\pi)|1|\mathbf{0}\}$, consisting of time reversal followed by a π spin rotation about an arbitrary in-plane axis. For coplanar structures with spins lying in the xy plane, the corresponding effective orbital time-reversal symmetry is $\{\mathcal{T}U_z(\pi)|1|\mathbf{0}\}$, which transforms a spin moment (S_x, S_y, S_z) to $(S_x, S_y, -S_z)$. Consequently, *without SOC, orbital altermagnetism is only possible for noncoplanar magnetic structures*, where no such effective orbital time-reversal symmetry exists.

Finally, we note an additional simplification in the SOC-free limit. Because spin-space operations W affect the orbital magnetic moment only through whether $\det(W) = +1$ or -1 , their action on M_{orb} reduces to a binary classification rather than depending on the detailed spin rotation itself. As a consequence, any nontrivial spin point group can be associated with a corresponding magnetic point group that captures the induced constraints on the orbital sector (see Table 7 in [129]). Therefore, when SOC is neglected, one may determine whether an orbital altermagnetism is symmetry-allowed by identifying the magnetic point group corresponding to the noncoplanar configuration’s nontrivial spin point group and then applying our magnetic-point-group screening results.

First-Principles Calculation Method

First-principles calculations are performed within the framework of density-functional theory (DFT) using the projector augmented-wave method and the Perdew-Burke-Ernzerhof-type exchange-correlation functional [118], as implemented in the Vienna *ab initio* simulation package (VASP) [119]. We set the cutoff energy of the plane-wave basis to be 520 eV and adapted a $15 \times 15 \times 1$ Γ -center k-mesh for the BZ sampling. SOC is included self-consistently in the calculations. To eliminate the spurious interaction between the 2D material and its images, a vacuum region of more than 12 Å along the z direction is set in the calculation. All crystal structures are fully optimized until the forces are less than 10^{-3} eV/Å and the change of the total energy is less than 0.01 meV. The correlation effect for the Cr $3d$ electrons and Mo $4d$ electrons is treated by the DFT+ U method with $U = 3.55$ and 2.4 eV [120, 121], respectively. To study the in-plane ferromagnetic configuration, we further performed constrained-moment calculations in VASP using the tags `I_CONSTRAINED_M` and `M_CONSTR` to align the spin moments along a chosen in-plane direction. To study the band geometric quantities such as the Berry curvature and orbital magnetization, we construct maximally localized Wannier functions (MLWFs) and derive a Wannier-based *ab initio* tight-binding model for each structure using the Wannier90 code [122]. Based on the Wannier representation, we calculate the Berry curvature $\Omega(\mathbf{k})$ and orbital magnetization of all states. All input structures, calculation parameters, and Wannier90 projectors used in this work are openly available in the Zenodo repository at [10.5281/zenodo.17506196](https://zenodo.org/record/17506196).

Numerical results of other candidate materials for orbital altermagnetism

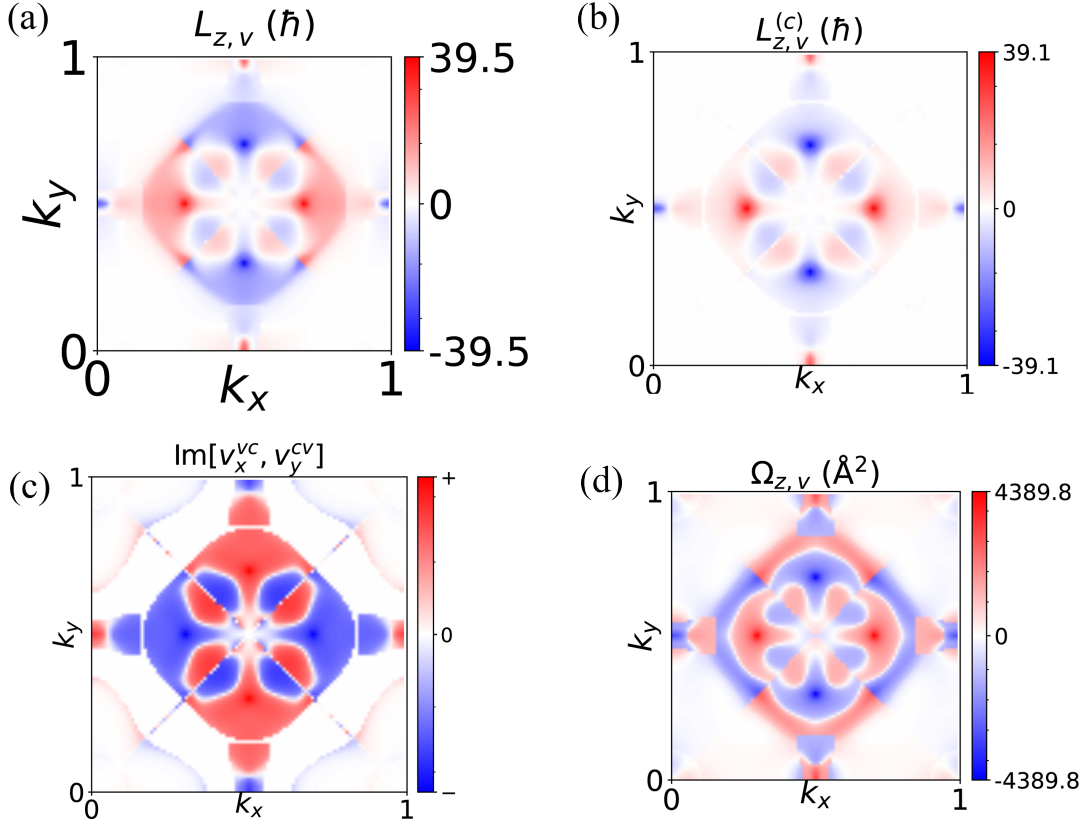


FIG. 5. Momentum-space distributions of quantities related to the orbital angular momentum for the highest valence band ($n = v$) and the lowest conduction band ($m = c$) of the MoO monolayer. (a) Distribution of the total $L_{z,v}$ in the Brillouin zone. (b) Distribution of the interband-resolved contribution $L_{z,v}^{(c)}$. (c) Distribution of $\text{Im}[v_x^{vc}, v_y^{cv}]$, showing the nodal lines separating regions of opposite sign. (d) Distribution of the Berry curvature $\Omega_{z,v}$ for comparison.

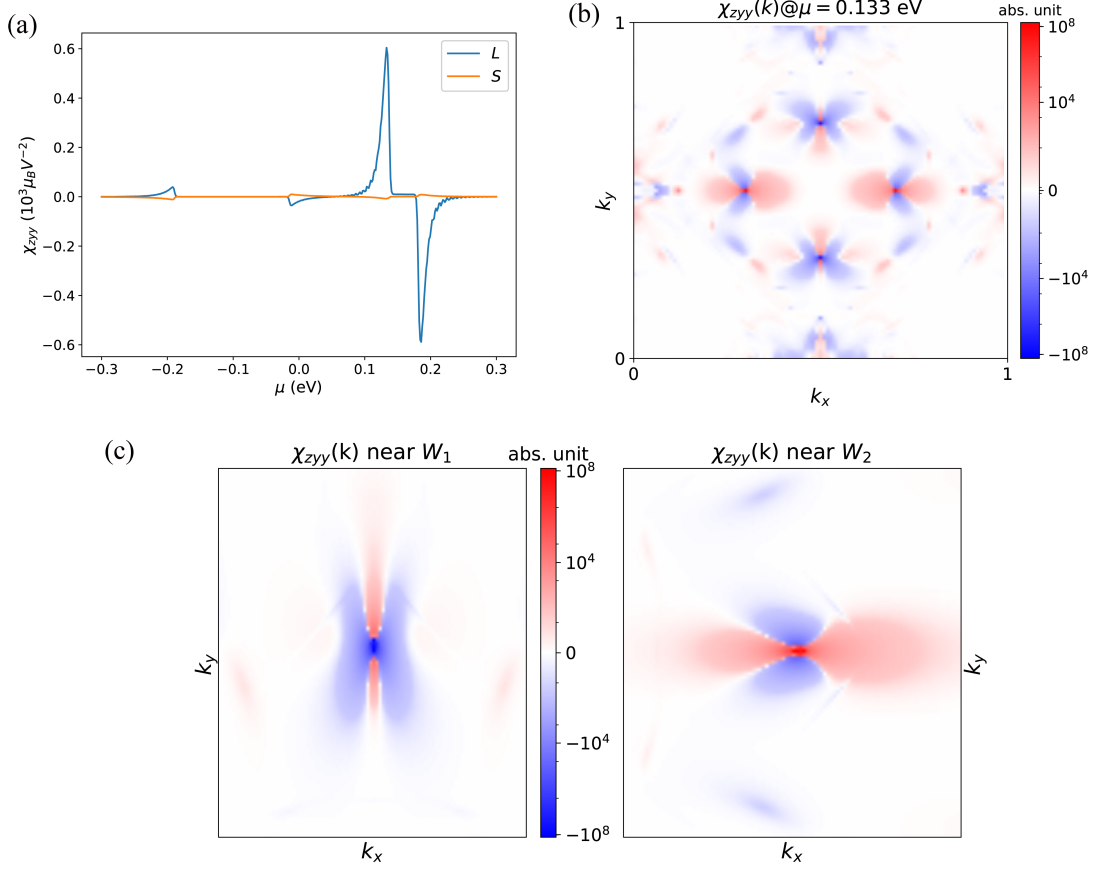


FIG. 6. (a) χ_{zyy} versus the chemical potential μ for monolayer MoO based on the first-principle calculations. (b) The distribution of $\chi_{zyy}(\mathbf{k})$ across the Brillouin zone, with the k_x and k_y expressed in reduced coordinates. (c) The distribution of $\chi_{zyy}(\mathbf{k})$ near the W_1 and W_2 , where μ is fixed at 0.133 eV.

Current-induced orbital magnetization in MoO monolayer

We first present the \mathbf{k} -space distribution of quantities related to the orbital angular momentum. Figure 5(b) shows the L_z of the highest valence band v mainly originates from the lowest conduction band c . Here we define:

$$M_{n\mathbf{k}}^{(m)} = -\frac{e}{2\hbar c} \text{Im} \frac{\langle u_{n\mathbf{k}} | \hat{\mathbf{v}} | u_{m\mathbf{k}} \rangle \times \langle u_{m\mathbf{k}} | \hat{\mathbf{v}} | u_{n\mathbf{k}} \rangle}{\varepsilon_{n\mathbf{k}} - \varepsilon_{m\mathbf{k}}} \quad (m \neq n), \quad (23)$$

$$L_{z,n}^{(m)}(\mathbf{k}) = -g_L \mu_B [M_{n\mathbf{k}}^{(m)}]_z.$$

To investigate the origin of the frequent sign changes of L_z in \mathbf{k} -space, we focus on the numerator in the expression $\text{Im}[v_x^{vc}, v_x^{vc}] = \text{Im}(v_x^{vc} v_y^{cv} - v_y^{vc} v_x^{cv})$, and plot its \mathbf{k} -space distribution for the c and v bands, as shown in Fig. 5(c). In momentum space, $\text{Im}[v_x^{vc}, v_x^{vc}]$ typically changes sign across the lines or regions where it vanishes. These zero-value contours divide the Brillouin zone into several sectors, and crossing such a line naturally leads to a reversal of the sign of the orbital magnetic moment. Similarly, the numerator of the Berry curvature has a comparable form. Therefore, we also plotted the Berry curvature distribution in \mathbf{k} -space, which shows a similar sign-reversal behavior.

Spin-orbit coupling opens a gap at the Weyl points W_1 and W_2 [95]. However, in the vicinity of these nearly degenerate points, the orbital angular momentum L_z remains strongly enhanced. Under an external field, these points contribute much more significantly to orbital magnetization than spin polarization. We calculated the nonlinear current-induced spin polarization (CISP) and current-induced orbital polarization (CIOP) in the MoO monolayer, as illustrated in Fig. 6(a). The results reveal that the orbital polarization is substantially stronger than the spin polarization. As shown in Fig. 6(b), W_1 and W_2 points represent the hotspot regions in the \mathbf{k} -space distribution of

$\chi_{zyy}(\mathbf{k})$. While the overall distribution follows the symmetry of the system, the local behaviors around W_1 and W_2 are quite different, as shown in Fig. 6. In particular, although the L_z distribution is linked by $C_{4z}\mathcal{T}$, the velocity matrix elements v_y at W_1 and W_2 lack such a symmetry connection, preventing cancellation between their contributions.

Figures 6(b,c) further demonstrate that the intrinsic CIOP is highly sensitive to band-energy differences, with the dominant contribution arising from the Fermi surface. This indicates that metallic or semimetallic 2D altermagnets are especially promising candidates for realizing large CIOP. Symmetry analysis shows that in MoO the out-of-plane CIOP exhibits a π -periodic angular dependence: $\chi_{zxx} = -\chi_{zyy}$ and $\delta X_z = \chi_{zxx} \cos 2\theta$, where the applied electric field is parametrized as $(E_x, E_y) = E(\cos \theta, \sin \theta)$.

Our calculations also indicate that applying 5% tensile strain in monolayer MoO shifts the W_1 and W_2 points close to the Fermi energy [95]. Since the SOC-induced gap is small, the associated orbital polarization L_z is expected to remain robust. This suggests that pressure or strain engineering offers a practical experimental route to probing strong orbital polarization effects in the MoO monolayer.

Monolayer altermagnet CrO

Figure 7 presents the crystal structure, electronic band structure, and L_z distribution in momentum space for monolayer CrO, demonstrating its characteristic orbital altermagnetic features.

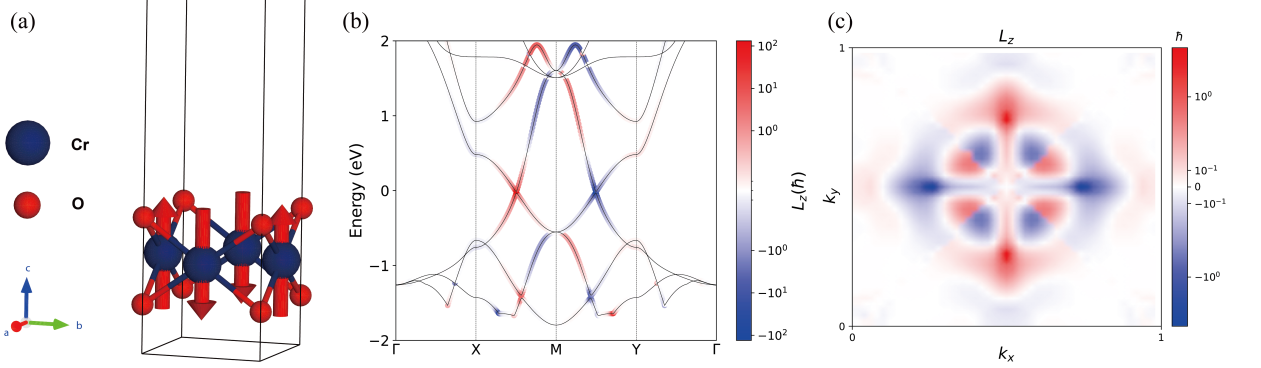


FIG. 7. (a) Side view of the lattice structure (red O atoms, blue Cr atoms). (b) Band structures of CrO, where the color represents the magnitude of L_z for the corresponding band and k -point. (c) The distribution of $L_z(\mathbf{k})$ across the Brillouin zone, with the k_x and k_y expressed in reduced coordinates. To better visualize the variation of L_z , all figures related to the $L_z(\mathbf{k})$ distribution use a logarithmic color scale.

Monolayer ferromagnet VS₂

The magnetic space group of monolayer ferromagnet VS₂ is $2/m$. As illustrated in Fig. 8, the inter-site currents between V and S atoms give rise to closed current loops within rhombic plaquettes consisting of two V atoms and their two adjacent S atoms. These current loops alternate in direction, with counter-circulating loops related by either the C_{2x} rotation or the m_x mirror symmetry.

Monolayer ferromagnet CuBr₂ with $s\parallel x$

Figure 9 shows the calculated band structure of CuBr₂ together with the corresponding L_z distribution in momentum space for the configuration with spin polarization along the x -axis. Figure 10 shows the curves of CIOP (CISP) in CuBr₂ for different spin orientations.

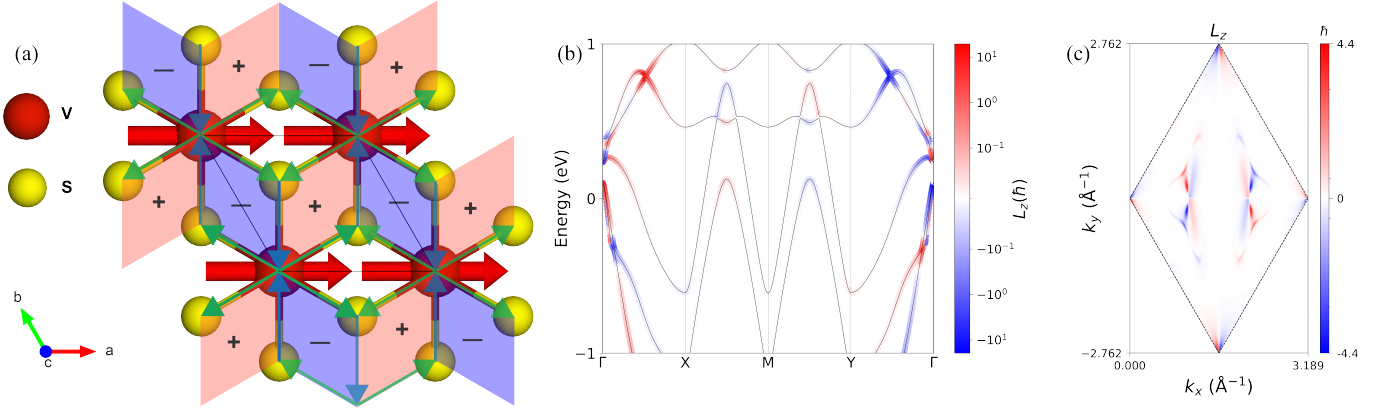


FIG. 8. (a) Crystal structure of monolayer VS₂ from the top view. The spin magnetic moments localized on the V atoms are annotated with arrows. Some inter-site currents between V and S atoms are marked with colored arrows. Blue corresponds to a current magnitude of $0.44 \mu\text{A}$, and green corresponds to $0.22 \mu\text{A}$. (b) Band structures of VS₂, where the color represents the magnitude of L_z for the corresponding band and k -point. (c) The distribution of $L_z(\mathbf{k})$ for the band 14 across the Brillouin zone. The boundaries of the Brillouin zone are marked with black dashed lines. To better visualize the variation of L_z , all figures related to the $L_z(\mathbf{k})$ distribution use a logarithmic color scale.

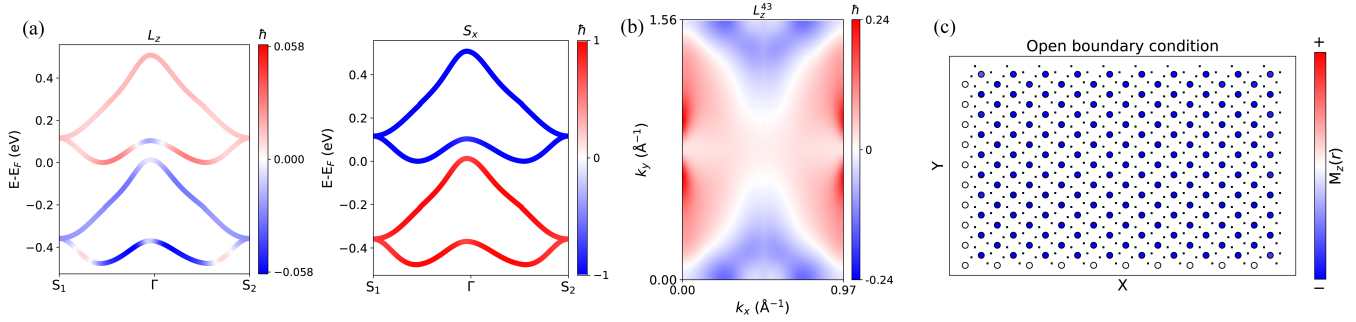


FIG. 9. (a) Band structures of CuBr₂ when spin is along x-axis, where the color represents the magnitude of L_z and S_x for the corresponding band and k -point. Here $S_1 = (0.5, 0.5)$ and $S_2 = (0.5, -0.5)$. (b) The distribution of $L_z(\mathbf{k})$ for the band 43 across the Brillouin zone. (c) The real-space distribution of orbital magnetic moments in a 10×10 system under open boundary conditions. Here we choose $\mu = 0$ eV.

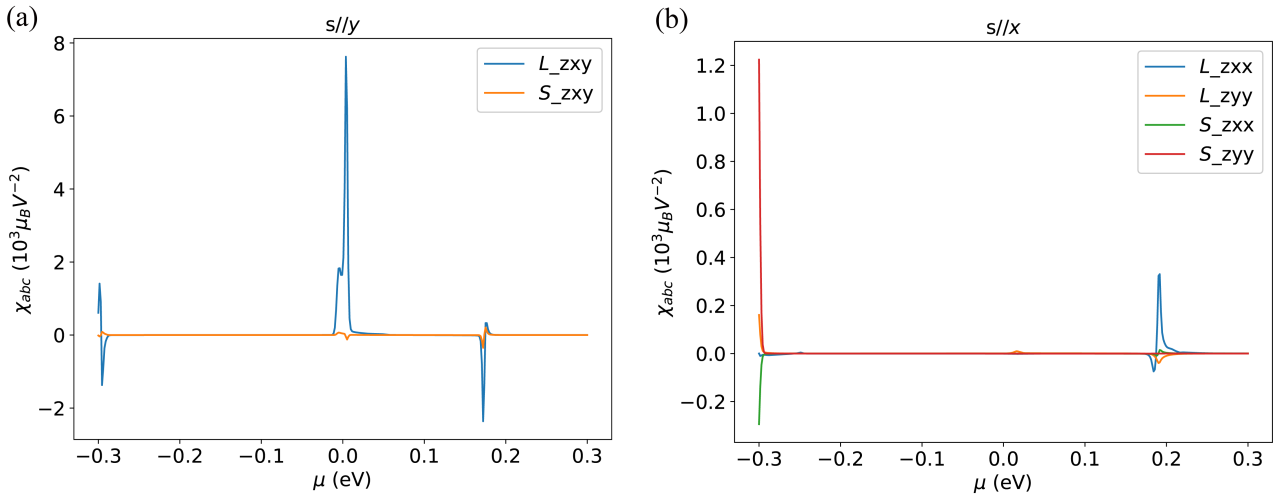


FIG. 10. χ_{abc} versus the chemical potential μ for monolayer CuBr₂ based on the first-principle calculations. (a) corresponds to spin polarization along y -axis, while (b) shows the case for x -axis polarization.

Discussion on experimental detection of orbital altermagnetism

In this section, we briefly discuss the possible experimental detection of the orbital altermagnetism, based on the recent developments on circular dichroic (angle-resolved) photoemission and nanoscale nitrogen vacancy (NV) centre quantum sensors.

Firstly, using circular dichroism (CD) in soft x-ray angle-resolved photoemission spectroscopy (ARPES), Brinkman, *et al.* reports the observation of the bulk orbital-angular-momentum texture and monopolelike orbital-momentum locking in the bulk electronic structure of chiral crystal CoSi [99]. By introducing the intrinsic chiral circular dichroism as a differential photoemission observable and a natural probe of chiral electron states, this approach can be effectively applied to detect chiral loop current induced orbital texture in \mathbf{k} -space. Accordingly, we expect that the d-wave altermagnetic order of orbital-angular-momentum texture can be measured using circular dichroism in bulk-sensitive soft x-ray ARPES, to provide additional evidence for our proposed orbital altermagnetic materials.

Secondly, for materials where orbital magnetization arises from loop currents or intra-unit-cell circulation, nanoscale magnetic field sensors such as nitrogen-vacancy (NV) centers in diamond offer a promising complementary technique. More recently, Xie and Nagaosa [100] demonstrated that NV magnetometry can detect the “local” stray magnetic fields generated by the fluctuation of orbital loop currents. This approach is particularly suitable for systems with relatively large sublattice separations, where the alternating orbital moments would generate measurable spatial variations in the stray magnetic field. In our context, scanning NV imaging could thus be employed to map the local magnetic field texture above the surface and indirectly confirm the predicted orbital altermagnetic pattern.
